

# The Role of MX Carbonitrides for the Particle-Stimulated Nucleation of Ferrite in Microalloyed Steel



EVELYN SOBOTKA , JOHANNES KREYCA , NORA FUCHS,  
TOMASZ WOJCIK , ERNST KOZESCHNIK ,  
and ERWIN POVODEN-KARADENIZ 

The role of titanium and vanadium carbonitrides (Ti,V)(C,N) of the MX series on the austenite-to-ferrite transformation in microalloyed steels and their potential of acting as pre-nuclei for intragranular ferrite nucleation is examined experimentally and by computational simulation. Thermal treatments and single-hit compression tests are performed on a dilatometer and a Gleeble® 3800 thermomechanical simulator to investigate the phase transition and precipitation sequences within microalloyed steel. The analysis of the microstructure and examination of formed precipitates is carried out by using scanning electron microscopy (SEM) and transmission electron microscopy (TEM). *In situ* observations are realized *via* high-temperature laser scanning confocal microscopy (HT-LSCM). The experimental results are compared to kinetic precipitation simulations for MX precipitates' particle-stimulated intragranular ferrite formation using an on-particle nucleation model for ferrite on the surface of the MX carbonitrides. A particular focus is the comparison of precipitation trends between non-deformed and deformed samples. The physically appropriate modeling of MX precipitation kinetics in combination with intragranular ferrite formation serves as a basis for future industrial process optimizations without extensive experimental work.

<https://doi.org/10.1007/s11661-023-07067-z>  
© The Author(s) 2023

## I. INTRODUCTION

THE term “microalloyed steel” derives from small additions of, conventionally, Ti, Nb, and V to low-carbon steels that cause grain refinement and precipitation strengthening by forming carbides and nitrides. The

application of different thermomechanical treatments strongly influences these strengthening effects of the microalloying elements.<sup>[1,2]</sup>

This work focuses on the experimental and computational examination of ferrite, which nucleates intragranularly on the surface of microalloy carbonitrides, and the effects of different thermomechanical treatments on it. The experimental analysis of the carbonitride precipitates and the austenite-to-ferrite transformation is compared to kinetic simulations using the simulation software MatCalc. We aim on controlling and predicting the competitive growth kinetics of intragranular ferrite and grain-boundary ferrite by appropriate thermomechanical treatments in order to optimize the microstructure properties of the final steel product.

### A. Fundamental Aspects of Carbonitrides in Microalloyed Steel

MX carbonitrides (M = Ti,Nb,V; X = C,N) have been shown to play a vital role for the grain refinement of microalloyed steel. Coarsening of austenite grains at high annealing temperatures can be reduced by solute elements like titanium, vanadium, and nitrogen, which enhance austenite grain refining. Solute V, for example,

---

EVELYN SOBOTKA is with the Christian Doppler Laboratory of Interfaces and Precipitation Engineering, Institute of Materials Science and Technology, TU Wien 1060 Vienna, Austria. Contact e-mail: evelyn.sobotka@tuwien.ac.at JOHANNES KREYCA is with the voestalpine Forschungsservicegesellschaft Donawitz GmbH 8700 Leoben, Austria. NORA FUCHS is with the Christian Doppler Laboratory of Interfaces and Precipitation Engineering, Institute of Materials Science and Technology, TU Wien and also with the Chair of Ferrous Metallurgy, Montanuniversitaet Leoben 8700 Leoben, Austria. TOMASZ WOJCIK and ERNST KOZESCHNIK are with the Institute of Materials Science and Technology, TU Wien 1060 Vienna, Austria. ERWIN POVODEN-KARADENIZ is with the Christian Doppler Laboratory of Interfaces and Precipitation Engineering, Institute of Materials Science and Technology, TU Wien and also with the Institute of Materials Science and Technology, TU Wien.

Manuscript submitted February 17, 2023; accepted April 22, 2023.

Article published online May 15, 2023

precipitates as V(C,N) in ferrite and pearlite, leading to precipitation strengthening. This strengthening effect is induced by fine particles, which form during the transformation to ferrite.<sup>[3–6]</sup> The deformation-induced formation of MX carbonitrides retards static recrystallization of austenite and, therefore, affects the austenite grain size.<sup>[1,7]</sup> During cooling, MX particles can induce nucleation of intragranular ferrite, enhancing the ferrite phase's refinement.<sup>[5]</sup>

Understanding the thermal stabilities of different MX carbonitrides and their mutual solubilities is an important prerequisite to establish a hierarchical precipitation order of different MX types for an optimized steel microstructure. The carbonitrides have the same face-centered cubic (fcc) crystal structure with similar lattice parameters, which promote their mutual solubilities.<sup>[2,3]</sup> Primary microalloy precipitates can directly form from molten steel,<sup>[8]</sup> while secondary (Ti/Nb/V)(C,N) carbonitrides nucleate at dislocations<sup>[9]</sup> as well as on the surface of other primary phases, such as MnS.<sup>[10]</sup> Irrespective of a ferritic or an austenitic steel matrix present, microalloy nitrides and mixed carbonitrides are thermodynamically more stable than the corresponding carbides. In terms of varying MX stabilities in the austenite depending on different solute atoms, Ti(C,N) shows the lowest solubility compared to other microalloy carbonitrides, such as Nb(C,N). V(C,N) has a rather high solubility in austenite, resulting in precipitation at lower temperatures.<sup>[11]</sup>

## B. Intragranular Ferrite Formation

In general, the heterogeneous nucleation of ferrite is driven by the reduced nucleation energy at interphase surfaces.<sup>[12]</sup> Kinetics of the austenite-to-ferrite phase transformation are not only regulated by the diffusion coefficients of the present elements but also by the mobility of the interfaces. The effective driving force for the austenite-to-ferrite transition is the sum of chemical and mechanical contributions. The chemical part is controlled by the actual compositions of ferrite and austenite next to the interface, while the mechanical factor, which reduces the effective driving force, is affected by the accommodation of volume strain due to an increasing number of carbonitrides within the steel matrix. Austenite-to-ferrite transformation reduces the strain fields created by carbonitrides and helps minimize the interfacial energy. The presence of precipitates can, therefore, enhance the formation of ferrite at higher temperatures.<sup>[13]</sup>

The formation of intragranular ferrite induces microstructure refinement and, thus, allows for the optimization of mechanical properties of microalloyed steel. The nucleation of intragranular ferrite in austenite is strongly affected by the steel composition and, thus, by differences of microalloying, the cooling conditions, the amount and type of non-metallic inclusions, and the prior austenitic grain size. The decisive factor for resulting fine ferritic-pearlitic structures is the concomitance of sufficiently large austenite grains and suitable precipitates, which act as nucleation sites for the ferrite.<sup>[14–17]</sup> Furthermore, deformation during thermal treatments initiates strain-induced precipitation of MX

(Ti,V)(C,N) carbonitrides, which can act as potential nucleation sites for ferrite within austenite grains.<sup>[18]</sup>

Intragranular ferrite (IGF) can be divided into the polygonal-shaped intragranular ferrite idiomorphs (PF) and the acicular ferrite (AF) with a needle-shaped appearance. The term acicular ferrite refers to ferrite laths that grow radially within the austenite matrix leading to a star-shaped morphology.<sup>[19]</sup> The microstructure of steels with a high volume fraction of AF features fine grains with high-angle grain boundaries, which restrain dislocation movement and crack extension, thus, leading to an excellent combination of strength and toughness.<sup>[20]</sup> Just as intragranular ferrite idiomorphs, acicular ferrite seems to nucleate within large prior austenite grains due to a high number density of intragranular nucleation sites, typically precipitates.<sup>[16,21]</sup> The actual nucleation site of ferrite accordingly depends on the total surface area ratio between these precipitates and the austenite grains.<sup>[12]</sup>

Park *et al.*<sup>[22]</sup> stated that a preferred tendency for AF formation, compared to PF, rises with an increasing particle size of the potential nucleation site. Contrary to polygonal intragranular ferrite, which holds no characteristic orientation relationship with austenite, acicular ferrite has a near Kurdjumov–Sachs (K–S) relationship with the prior austenite phase. The fcc particles, which AF nucleates on, hold a Baker–Nutting relationship with the ferrite phase.<sup>[23,24]</sup> The lattice mismatch of VX and intragranular ferrite (0.032 for VC, 0.018 for VN) is significantly smaller than that of TiX (0.076 for TiC, 0.047 for TiN) or NbX (0.1 for NbC, 0.16 for NbN) and ferrite.<sup>[17]</sup> The crucial factor for the intragranular nucleation of ferrite on precipitates is coherent, low-energy interfaces, which is realized by a small atomic mismatch. This is the case for V(C,N) particles, which have, therefore, the largest potential to serve as nucleation site for PF or AF. Other preconditions for acicular ferrite formation are a low-carbon content of the steel and solute manganese in the matrix.<sup>[12]</sup>

Previous studies<sup>[20,25]</sup> compared the nucleation potential of several types of precipitate complexes. In most instances, sole single-phase oxides (Al<sub>2</sub>O<sub>3</sub>, MnO)<sup>[12]</sup> and sulfides (MnS) alone do not represent active AF nucleation sites in steel. In contrast, several studies<sup>[10,26,27]</sup> reported that intragranular ferrite nucleates on vanadium carbonitride particles (~ 0.2 μm), which have formed on manganese sulfides (~ 1 μm) during the preceding heat treatment. Recently, it has been reported by Zajac *et al.*<sup>[4,28]</sup> that V(C,N) would be the most effective nucleation site for intragranular ferrite, either as precipitate complex in a mixture with MnS, or as strain-induced precipitation of *sole* vanadium carbonitrides. Additionally, vanadium carbonitrides, acting as pre-nuclei for intragranular ferrite, can themselves precipitate on already existing TiN.

## II. MATERIALS AND METHODS

Within the framework of this study, precipitation kinetics of MX and ferrite in a microalloyed industrial steel with low-carbon content are investigated. Table I

**Table I. Chemical Composition**

Element	C	Mn	Ti	Nb	V
Concentration [Weight Percent]	0.20	1.40	< 0.01	< 0.01	0.10

gives the chemical composition of the examined material, which, in agreement to the expected benefits that have been discussed above, contains higher amounts of the element vanadium in comparison to titanium and niobium.

### A. Experiments

#### 1. Austenite-to-ferrite transformation investigations from dilatometry and HT-LSCM

The ferrite formation during cooling after an isothermal holding step of different holding times at 1153 K is traced *via* dilatometry (DIL 805). Further, the effect of deformation is investigated by single-hit compression tests. Figure 1 depicts the schematic schedule of this experimental series. Cylindrical specimens with 5 mm diameter and 10 mm length are used. The samples are solution annealed at 1553 K for 600 seconds, cooled down to 1153 K, and either immediately quenched or held for 125/1600 seconds before cooling to room temperature. A cooling rate of  $7 \text{ K s}^{-1}$  was chosen using argon as quenching medium. Cooling with  $\sim 7 \text{ K s}^{-1}$  has been shown in an earlier study<sup>[14]</sup> to favor the formation of acicular ferrite in low-carbon microalloyed steels.

The treatment of the isothermal single-hit compression tests using the dilatometer remains the same, except for the additional deformation after 25/1500 seconds holding with  $0.01 \text{ s}^{-1}$  strain rate to a true strain of 1. With these conditions chosen, the overall holding time at the test temperature corresponds to the non-deformation experiments, and comparability is, thus, ensured.

*In situ* information about the austenite-to-ferrite formation and the austenite grain growth is attained, employing the thermal etching effect<sup>[29]</sup> in high-temperature laser scanning confocal microscopy (HT-LSCM) using the type VL 2000 DX by Lasertec in combination with a high-temperature furnace SVF17-SO by YONEKURA. Samples of the geometry  $5 \times 5 \times 1.5 \text{ mm}$  are cut, ground, and polished. For the HT-LSCM investigations, the heat treatments of Figure 1, without deformation, are performed. The austenite grain size evolution is examined by using the “linear intercept” method according to.<sup>[30,31]</sup> Resulting ferrite phase fractions are quantified after the test by optical light microscopy (LOM). For analysis of the acicular ferrite phase fraction of the HT-LSCM samples, a computerized data evaluation of the LOM images, developed by Loder *et al.*,<sup>[15]</sup> is applied.

#### 2. Precipitate analysis from Gleeble® experiments, characterized with SEM and TEM

To investigate the impact of carbonitrides on the examined material, compression tests with  $0.01 \text{ s}^{-1}$

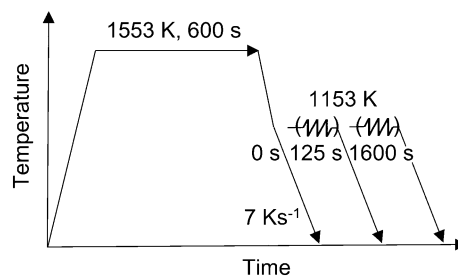


Fig. 1—Schematic thermal treatment for austenite-to-ferrite transformation experiments.

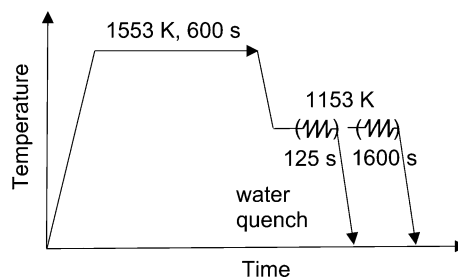


Fig. 2—Schematic thermomechanical rolling pattern for single-hit Gleeble compression tests.

strain rate to a true strain of 1 are performed on a Gleeble® 3800 thermomechanical simulator, according to the processing scheme of Figure 2. Cylindrical samples with 10 mm diameter and 15 mm length are employed. The chosen treatment is actually the same as for the dilatometry experiments, except that water quenching is applied from 1153 K to room temperature in the Gleeble® tests. Due to this rapid cooling, the state of the carbonitrides at the isothermal test temperature is “frozen.” The role of deformation on the precipitate evolution is deciphered by comparing these experimental results with the ones from the same heat treatments without deformation.

Microstructures are examined by LOM using a Zeiss AxioImager. The analysis of the chemical phase compositions and particle size distribution of the precipitates is done *via* scanning electron microscopy (SEM) on a Zeiss Sigma 500 VP and transmission electron microscopy (TEM) using a FEI Tecnai F20 instrument.

For LOM and SEM analyses, the specimens are cut, hot embedded with conductive resin, ground, and polished. The surface structure is made visible by 5 pct nital etching for LOM and SEM. The chemical composition of the particles is determined by energy-dispersive X-ray spectroscopy (EDX). The prior austenite grain boundaries are analyzed on the basis of DIN EN ISO 643<sup>[32]</sup> using “Bechet Beaujard” etching (100 mL picric

acid, 1.6 g CuCl<sub>2</sub>, and 0.5 mL aegon) as well as the etching method of “Görens” (40 cm<sup>3</sup> distilled water, 60 cm<sup>3</sup> ethanol, and 20 g FeCl<sub>3</sub>).<sup>[33]</sup>

For TEM analyses, two different kinds of sample preparations are used. (1) To investigate the precipitate sizes, carbon extraction replicas<sup>[34]</sup> are prepared. After embedding the sample in a bright resin, they are ground, polished, and nital etched. A thin film of carbon is deposited on the sample surface, which is carefully cut into small squares (~ 1 mm<sup>2</sup>). Etching is repeated until the carbon replica pieces, which extract the precipitates, lift from the matrix. The carbon replicas are subsequently placed on Cu/Au grids, which are mounted in a suitable specimen holder. (2) Thin-film samples provide information on the nucleation sites of the precipitates within the matrix. Disks of 1 mm thickness are cut from the specimen, ground to ~ 60 μm, and are electrochemically etched with an appropriate electrolyte comprising 7 pct perchlorate, 51 pct ethanol, 31 pct butanol, and 11 pct ethylene glycol monobutyl ether at 263 K with 26 V.

The average number density and size of precipitates from scanning transmission electron microscopy in combination with high-angle annular dark field imaging (STEM-HAADF) are evaluated using the software ImageJ.<sup>[35]</sup> Color threshold adjustments are iterated, to distinguish the precipitates from the matrix by their different contrasts. Quantification of the chemical composition of the particles is realized with EDX and energy-filtered transmission electron microscopy (EFTEM).

## B. Simulation

The mean-field software MatCalc, which employs thermodynamic<sup>[36]</sup> and diffusion mobility<sup>[37]</sup> databases, is applied in the simulation of precipitation and microstructure evolution for the experimental heat and thermomechanical treatments. For the prediction of MX and ferrite evolution, nucleation and growth kinetics modeling are combined with the modeling of the dislocation density evolution<sup>[38–40]</sup> and recrystallization kinetics.<sup>[41–45]</sup> As ferrite nucleates also on the surface of MX particles, the physically correct adjustment of the following model parameters for the carbonitride phases is essential. Within this study, the volumetric misfit parameter, the regular solution critical temperature, the inner particle diffusion factor, and strengthening parameters in the case of recrystallization are physically assessed. In the following, their origin and selected equations, explaining their background, are discussed.

### 1. Volumetric misfit parameter $V_{eff\_mis}$

The formation of precipitates in the steel matrix is calculated on the basis of the classical nucleation theory,<sup>[46]</sup> adapted for complex phases (*i.e.*, precipitates which consist of multiple phases) in multicomponent systems.<sup>[47,48]</sup> The transient nucleation rate  $J$ ,<sup>[46]</sup> which describes the formation of a nucleus per unit volume and time, is given by

$$J(t) = Z\beta N \cdot \exp\left(\frac{-\Delta G^*}{kT}\right) \cdot \exp\left(\frac{-\tau}{t}\right), \quad [1]$$

where  $Z$  is the Zeldovich factor, it takes the destabilization of the nuclei by thermal excitations into account. The parameter  $\beta$  represents the attachment rate at which atoms are added to the critical nucleus,  $N$  the number of atomic nucleation sites of a particular type per unit volume,  $\Delta G^*$  the Gibbs free energy for forming a critical nucleus,  $k$  the Boltzmann constant,  $T$  the temperature,  $\tau$  the incubation time for establishing steady-state nucleation conditions, and  $t$  the isothermal reaction time. The Gibbs free energy for the formation of a critical nucleus<sup>[46]</sup> is calculated by

$$\Delta G^* = \frac{16\pi}{3} \frac{\gamma^3}{(\Delta G_{vol} + \Delta G_S)^2}, \quad [2]$$

where  $\gamma$  represents the interfacial energy between matrix and particle,  $\Delta G_{vol}$  is the chemical driving force per unit volume of the precipitate, and  $\Delta G_S$  describes the misfit strain energy, which can be viewed as the mechanical contribution reducing the driving force. The misfit strain energy  $\Delta G_S$  per unit volume of precipitate<sup>[46]</sup> is given by

$$\Delta G_S = \frac{E}{1-\nu} \varepsilon^2, \quad [3]$$

$$E = 2\mu(1+\nu), \quad [4]$$

where  $E$  is the Young modulus,  $\nu$  the Poisson ratio of the matrix,  $\varepsilon$  the linear misfit strain, which is equal to 1/3 of the transformation volume change, and  $\mu$  the shear modulus. The linear misfit strain  $\varepsilon$ <sup>[46]</sup> can be derived from  $V_m^P$  and  $V_m^M$ , which describe the molar volumes of the precipitate and the matrix, respectively:

$$\varepsilon = \frac{1}{3} \frac{V_m^P - V_m^M}{V_m^M}. \quad [5]$$

By inserting Eq. [5] into Eq. [3], it becomes clear that the precipitation of MX carbonitrides has an impact on  $\Delta G_S$ , as follows. An increase of the misfit strain energy (Eq. 3) due to a high volumetric misfit between precipitates and matrix (Eq. 5) can directly decrease the driving force for the precipitation (Eq. 2), resulting in a reduction of the nucleation rate (Eq. 1).

Fischer *et al.*<sup>[49]</sup> noted that simultaneous precipitate growth and misfit stress relaxation can occur. Lattice defects, such as dislocations and grain boundaries, have a severe impact on the misfit strain energy and result in local stresses. For the modeling of precipitation at grain boundaries, no volumetric misfit has to be considered because of the stress relaxation due to vacancy creation and annihilation at the interface between the particle and the matrix. Contrary, the simulation of particle nucleation at dislocations (such particles may appear homogeneously distributed within the steel microstructure) requires a constrained volumetric misfit parameter<sup>[49,50]</sup> since the matrix and precipitates are elastically stressed, and the volumetric mismatch decreases.<sup>[51]</sup> The

choice of the parameter has a major impact on precipitation kinetics since an increase of the volumetric mismatch (in the case of the unconstrained volumetric mismatch between MX and steel matrix  $> 0.2$ ) can retard the nucleation of precipitates to longer times by several orders of magnitude. It is clear that such a high mismatch prevents the precipitation of MX coherently in the bulk, and they are found preferably at dislocations. Despite the strong misfit of, *e.g.*, NbC in all directions with the iron matrix,<sup>[52,53]</sup> in the case of a *theoretic* fully homogeneous nucleation, the effective constrained misfit for numerical simulations is negligibly small, and it, thus, has no significant impact on precipitation kinetics, according to Radis *et al.*<sup>[54]</sup>

For the following numerical simulations of nucleation processes at dislocations, the constrained misfit between particle and matrix is included. Table II lists the values of the lattice parameters  $a$ , the molar volumes, and the resulting calculated unconstrained volumetric misfits of the relevant phases:

$$V_{\text{mis}} = \frac{V_{\text{m}}^{\text{P}} - V_{\text{m}}^{\text{M}}}{V_{\text{m}}^{\text{M}}}. \quad [6]$$

The molar volume of the individual phases is calculated from

$$V_{\text{m}} = \frac{a^3 \cdot N_{\text{a}}}{n}, \quad [7]$$

where  $N_{\text{a}}$  describes the Avogadro constant and  $n$  the number of atoms inside the unit cell. The ranges of  $V_{\text{mis}}$  origin from the different molar volume data found in the literature.

Table II indicates a significant difference between the volumetric misfits of the carbonitrides. Nb(C,N) shows the largest mismatch, followed by Ti(C,N) and eventually V(C,N). It is notable that the volumetric misfit between austenite and ferrite is negligible. For precipitation simulation, the constrained volumetric misfit  $V_{\text{eff\_mis}}$  values are consistently estimated to be 1/10 of the evaluated unconstrained values. This value was determined by iterative adjustment from kinetic

simulations and matches the values from the literature,<sup>[17]</sup> as discussed in Section I.B.

## 2. Regular solution critical temperature $T_{\text{crit}}$

Mixing of atoms along the interfaces between two phases adds additional entropic contributions to a coherent planar sharp interfacial energy  $\gamma$ , resulting in a corresponding lower dilute interfacial energy. Sonderegger *et al.*<sup>[62]</sup> described how the general broken-bond (GBB) model can be applied for the computational assessment of diffuse interface energies between small precipitates and the alloy matrix of a multicomponent system. The two key equations of this approach are presented in the following Eqs. [8] and [9]:

$$\gamma = \alpha(r) \cdot \beta\left(\frac{T}{T_{\text{crit}}}\right) \frac{n_{\text{S}} \cdot z_{\text{S}}}{N_{\text{a}} \cdot z_{\text{L}}} \Delta H_{\text{sol}}, \quad [8]$$

$$\begin{aligned} \beta\left(\frac{T}{T_{\text{crit}}}\right) = & 8.4729 \cdot \left(\frac{T}{T_{\text{crit}}}\right)^6 - 26.691 \cdot \left(\frac{T}{T_{\text{crit}}}\right)^5 \\ & + 32.717 \cdot \left(\frac{T}{T_{\text{crit}}}\right)^4 - 17.674 \cdot \left(\frac{T}{T_{\text{crit}}}\right)^3 \\ & + 2.2673 \cdot \left(\frac{T}{T_{\text{crit}}}\right)^2 - 0.09 \cdot \left(\frac{T}{T_{\text{crit}}}\right) + 1.00047632, \end{aligned} \quad [9]$$

where the function  $\alpha(r)$  takes the effect of phase boundary curvature into account,  $\beta(T/T_{\text{crit}})$  describes the diffuse interface energy reduction,  $n_{\text{S}}$  is the number of atoms per unit interfacial area,  $z_{\text{S}}$  is the effective number of broken bonds across the interface,  $N_{\text{a}}$  is the Avogadro's number,  $z_{\text{L}}$  is the effective coordination number, and  $\Delta H_{\text{sol}}$  is the enthalpy of solution.

Equations [8] and [9] indicate that the contribution of the diffuse interface to the interfacial energy between matrix and precipitates is controlled by the regular solution critical temperature  $T_{\text{crit}}$ , which can be estimated from the closing temperature of miscibility gaps of fcc Fe-MX phase diagrams. The value of  $T_{\text{crit}}$  represents the maximum temperature of the according phase boundary or, in other words, the highest temperature of the thermodynamically stable regular solution.<sup>[63]</sup> In the present case,  $T_{\text{crit}}$  describes the critical

**Table II. Volumetric Misfit of MX Carbonitrides and Parameters Needed for Calculation**

	$a$ [nm]	$V_{\text{m}}$ [ $10^{-6} \text{ m}^3 \text{ mol}^{-1}$ ]	Source	$V_{\text{mis}}$ in Ferrite	$V_{\text{mis}}$ in Austenite
TiC	0.433, 0.432	12.21	[2, 55, 56]	0.65 to 0.72	0.66 to 0.72
TiN	0.425	11.59, 11.47	[2, 55, 56]	0.55 to 0.64	0.56 to 0.63
NbC	0.447	13.45	[2, 57]	0.82 to 0.90	0.83 to 0.89
NbN	0.439	12.72	[2]	0.72 to 0.80	0.73 to 0.79
VC	0.416	10.84, 10.81	[2, 58]	0.46 to 0.53	0.47 to 0.52
VN	0.409 to 0.417	10.30 to 10.92, 10.52	[2, 58]	0.39 to 0.54	0.40 to 0.54
Ti(C,N)	0.428	11.83	[56]	0.60 to 0.67	0.61 to 0.66
Nb(C,N)	0.440	12.80	[9]	0.73 to 0.81	0.74 to 0.80
V(C,N)	0.414	10.65	[58]	0.44 to 0.50	0.45 to 0.50
Ferrite	0.287	7.12, 7.08 to 7.39	[59, 60]	—	— 0.04 to 0.04
Austenite	0.365	7.25 to 7.35, 7.11	[58, 59, 61]	—	—

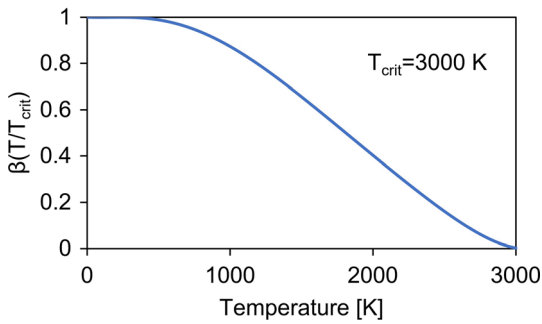


Fig. 3—Dependency of the diffuse interface energy reduction factor on temperature for  $T_{crit} = 3000$  K.

**Table III.**  $T_{crit}$  of MX Carbonitrides in Austenitic Fe-Matrix

	$T_{crit}$ [K]
TiC	—
TiN	4200
NbC	3300
NbN	3200
VC	2100
VN	3300
Ti(C,N)	4200
Nb(C,N)	3250
V(C,N)	2700

temperature where the interfacial energy  $\gamma$  between matrix and theoretic bulk MX diminishes due to the diffuse character of the interface.<sup>[63]</sup> The temperature dependency of the diffuse interface energy reduction factor is exemplarily shown in Figure 3 for  $T_{crit} = 3000$  K, as evaluated by the use of Eq. [9].

Within this work, Calphad-assessed phase diagrams of microalloying elements in combination with carbon and nitrogen, as implemented in the thermodynamic MatCalc database *mc\_fe*,<sup>[36]</sup> are used for the determination of  $T_{crit}$ ; Table III, of the investigated alloy. Thermo-Calc<sup>[64]</sup> is particularly suitable for the evaluation of peak temperatures of miscibility gaps and is utilized to determine it for the assessed MX thermodynamics in the steel database *mc\_fe*. Only perfectly closed miscibility gaps in the thermodynamic computations provide a realistic derivation of  $T_{crit}$ . Uncertainties of appropriate  $T_{crit}$  values remain, representing limitations of the predictive power for the  $T_{crit}$  approach. For the cases Fe–TiC, Fe–NbC, and Fe–VN, only rough estimates can be given due to difficulties in the modeled miscibility behavior (*e.g.*, the Calphad-assessed miscibility gap does not completely close towards high temperatures) between the austenitic Fe-base matrix and MX. The computed phase diagrams are depicted in the appendix, see Figures A1, A2, A3, A4, A5, and A6. Further, since the carbonitride phases are not completely coherent, the diffuse interface effect may be smaller, and the effective values of  $T_{crit}$  may therefore be higher than theoretically predicted ones.

### 3. Inner particle diffusion factor IPDF

The miscibility behavior among (Ti,Nb,V)(C,N) carbonitrides, which consists of the potential mutual mixing between three metallic atoms, two interstitials, and combinations, is complex and the “transfer” from the thermodynamic base to predictive kinetic simulation is not straight-forward. This is also indicated by the fact that the stabilization of MX particles during different thermomechanical treatments is not controlled by equilibrium thermodynamics alone. The Calphad-computed co-existence of MX compounds can largely deviate from the experimental observations. We found out that in order to realize the nucleation of separate carbonitrides, the diffusion coefficients within the particles also play an important role and have to be considered in the kinetic parameter setup. This is in line with previous findings by Stechauner *et al.*<sup>[63]</sup>, who examined the precipitation of Cu in ferrite and stated that the inner particle diffusion factor (*IPDF*) would play a vital role in the chemical composition of the nuclei after specific holding times, and so-to-say on their “evolution path” from non-equilibrium to equilibrium. Interestingly, at the same time, the factor has hardly any impact on the radius and number density of the formed phase.

By default, in MatCalc, the diffusion of the elements within a formed particle, *IPDF*, is directly related to the diffusion coefficient of the surrounding matrix as a ratio factor of 0.01. For our kinetic simulations, an interstitial inner diffusion in precipitate factor of  $\leq 0.01$  is essential for the individual modeling of MX particles. Moreover, since the activation energy for diffusion in the face-centered cubic austenite matrix has higher values than for the body-centered cubic ferrite,<sup>[65]</sup> diffusion in acicular ferrite, as well as grain-boundary ferrite, also has to be reduced. Within this work, the *IPDF* for AF, as well as GBF, is set as 0.15. Compared to the austenite matrix, the diffusivity within the ferrite phases is reduced by 85 pct.

### 4. Strengthening parameters A, B, and C

To describe microstructure strengthening based on the dislocation density evolution during deformation, an extended<sup>[66]</sup> substructure model by Kocks and Mecking<sup>[67,68]</sup> is applied. The three terms of the simulation model<sup>[66]</sup> control the generation of dislocations (*A*), dynamic recovery (*B*), and static recovery (*C*):

$$\frac{\partial \rho}{\partial \varphi} = \frac{M}{bA} \sqrt{\rho_{tot}} - 2BM \frac{d_{crit}}{b} \rho_{tot} - 2CD_{eff} \frac{Gb^3}{\varphi kT} (\rho_{tot}^2 - \rho_{eq}^2), \quad [10]$$

where  $\rho$  describes the mean excess dislocation density,  $\varphi$  the true strain,  $M$  the Taylor factor,  $b$  the Burgers vector,  $\rho_{tot}$  the total dislocation density,  $d_{crit}$  the critical annihilation distance between two dislocations,<sup>[41]</sup>  $D_{eff}$  the effective diffusion coefficient, which accounts for pipe diffusion due to dislocations,<sup>[65]</sup>  $G$  the shear modulus,  $\dot{\varphi}$  the strain rate,  $k$  the Boltzmann constant,  $T$  the temperature, and  $\rho_{eq}$  the dislocation density of a well-annealed microstructure. The evaluation of the parameters *A*, *B*, and *C* for microalloyed steel is

**Table IV. Parameter Symbols and Values for the MatCalc Simulation Models**

Symbol	Name	Value	Unit	Literature Source
$V_{\text{eff,mis,MX}}$	effective constrained volumetric misfit of (Ti/Nb/V)(C,N)	0.061/0.074/0.045	—	this work
$T_{\text{crit,MX}}$	highest possible solution temperature of (Ti/Nb/V)(C,N)	3800/2800/2300	°C	[74]
$T_{\text{crit,MnS}}$	highest possible solution temperature of MnS	2130	°C	[75]
$IPDF_{\text{MX}}$	inner particle diffusion factor of (Ti/Nb/V)(C,N)	0.01/0.0006/0.01	—	this work
$IPDF_z$	inner particle diffusion factor of AF and GBF	0.15	—	this work
$A/B/C$	strengthening parameters	$31.8/8.1/2.6 \times 10^{-6}$	—	[69]

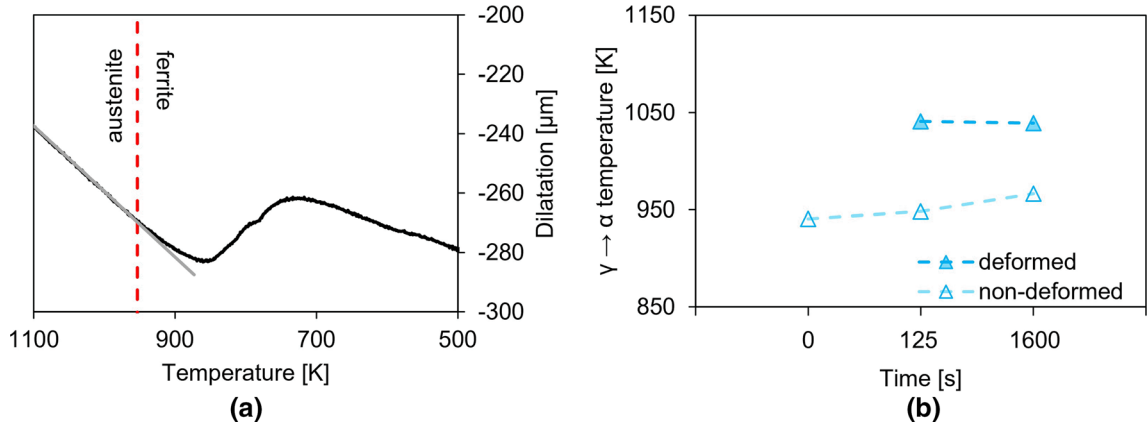


Fig. 4—(a) Exemplary determination of austenite-to-ferrite transformation temperature using dilatometry; (b) Transformation temperatures of deformed and non-deformed material with varied holding time at 1153 K using dilatometer.

discussed in a recent publication by the authors.<sup>[69]</sup> The values of  $A$ ,  $B$ , and  $C$  are derived from physical parameters, which can correctly assess the examined experimental flow curves. Knowledge of the dislocation density evolution is necessary to describe the effect of strain-induced precipitation.

### 5. Particle-stimulated nucleation of phases

Both primary and secondary phases play a vital role in the formation of epitaxial ferrite. In the simulation, the characterization of primary precipitates and the trend of phase fractions and compositions of all phases present during solidification are computed with the Scheil–Gulliver method.<sup>[70–72]</sup> Besides the nucleation of secondary (Ti,Nb,V)(C,N) carbonitrides at dislocations,<sup>[9]</sup> the particles also form on primary phases. For the heterogeneous nucleation of MX precipitates and ferrite on the surface of pre-existing particles, the so-called on-particle nucleation model in MatCalc is used. The new phase nucleates at the phase boundary between the present parent precipitate, which acts as a catalyst for the formation, and the matrix. The particle distribution of the parent phases is not affected by the nucleation of the new precipitate. The nucleation process is limited by the diffusional transport of atoms in the matrix. Within this particle-related transformation, each atom on the surface of the parent phase acts as a potential nucleation site. The power of MatCalc is that *multiple* different phases can be selected as parent particles. The overall number of nucleation sites  $N_{\text{nucl}}$  is

obtained by the total interfacial area of all parent particles  $A_{\text{int}}$  divided by the mean area of one single atom  $A_{\text{at}}$ , Eqs. [11] through [13].

$$N_{\text{nucl}} = A_{\text{int}}/A_{\text{at}}, \quad [11]$$

$$A_{\text{int}} = \sum_{i,j} p_i 4\pi r_j^2, \quad [12]$$

where  $p$  is the size class of a precipitate bigger than the (user-defined) minimum nucleation radius and  $r$  is the radius of the size class.  $A_{\text{at}}$  is calculated *via* the square of the lattice constant,  $A_{\text{at}} = a^2$ , in combination with Eq. [7]:

$$A_{\text{at}} = \left( \frac{V_m \cdot n}{N_a} \right)^{2/3}. \quad [13]$$

The nucleation rate  $J$  is otherwise evaluated as identical to the transient homogeneous nucleation rate from Eq. [1], with  $N$  replaced by  $N_{\text{nucl}}$ .

### 6. MatCalc simulation parameters

Table IV lists the applied parameters needed for the simulation of precipitation kinetics. For the simulation of austenite grain growth, a model presented by Rath and Kozeschnik<sup>[73]</sup> is used. Detailed information about the applied models for the dislocation density evolution in combination with recrystallization is given in published work by the authors of this study.<sup>[69,74]</sup>

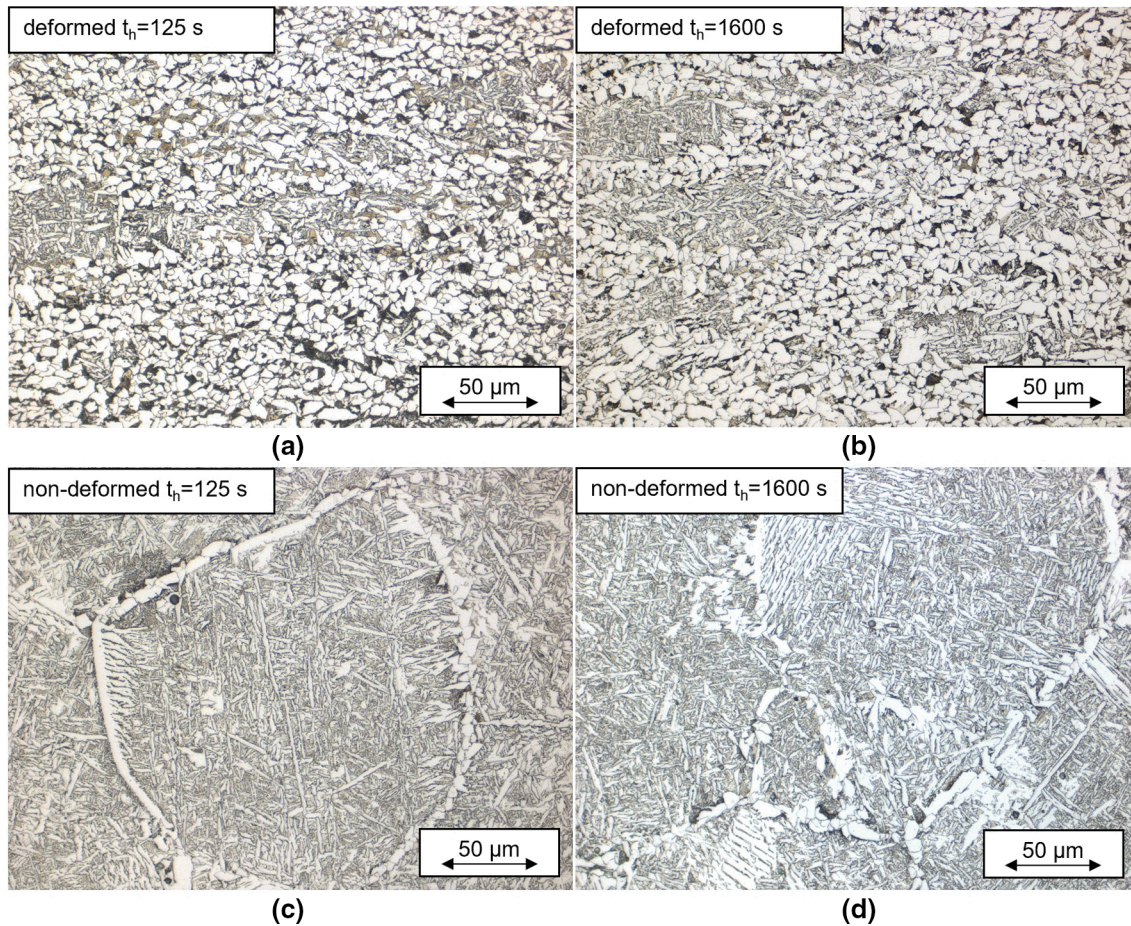


Fig. 5—Light microscopy images of dilatometer samples with various holding times at 1153 K, after cooling with  $7 \text{ K s}^{-1}$  to room temperature. (a) Deformed, 125 seconds holding; (b) deformed, 1600 seconds holding; (c) non-deformed, 125 seconds holding; (d) non-deformed, 1600 seconds holding.

### III. RESULTS AND DISCUSSION

The impact of varying intermediate holding times at the investigation temperature on the precipitation sequences and ferrite formation during cooling is presented.

#### A. Experiments

##### 1. Austenite-to-ferrite transformation investigations from dilatometry and HT-LSCM

*a. Dilatometry* Figure 4 depicts the results from dilatometer experiments. The starting temperature of the austenite-to-ferrite transformation is determined by plotting the dilatation signal against temperature, Figure 4(a). Figure 4(b) shows that in the experiments without deformation, a shorter holding time of 125 seconds at 1153 K results in a slightly lower transition temperature (948 K) compared to a prolonged time of 1600 seconds (966 K). This is explained by the increasing amount of potential (Ti,Nb,V)(C,N) nucleation sites due to the ongoing precipitation process. In the following, the precipitate distribution for the two material states, the state after shorter vs the one after longer

holding time, is detailed. This acts as a validation base for the subsequent MatCalc simulation, Section III.B.

Deformation has a substantial impact on the transition temperature. The temperature is found to be  $\sim 1040 \text{ K}$ , irrespective of the chosen holding times. It should be noted that deformation tests without holding prior to compression are not executed as the temperature needs sufficient time ( $\sim 20$  seconds) to stabilize at 1153 K. Based on the elevated transformation time of the deformation experiments, it is presumed that compression increases the number of dislocations serving as available nucleation sites to such a high level that pre-nuclei only play a minor role for the ferrite precipitation.

Figure 5 shows that deformation enhances ferrite formation, independently of the holding times. The images of the non-deformed samples further show that different intermediate holding times do not have a significant impact on the final microstructure. Grain-boundary ferrite can be clearly distinguished from acicular ferrite within the prior austenite grains.

*b. HT-LSCM* HT-LSCM delivers important complementary information to the dilatometric transformation analysis. It allows one to directly observe whether the



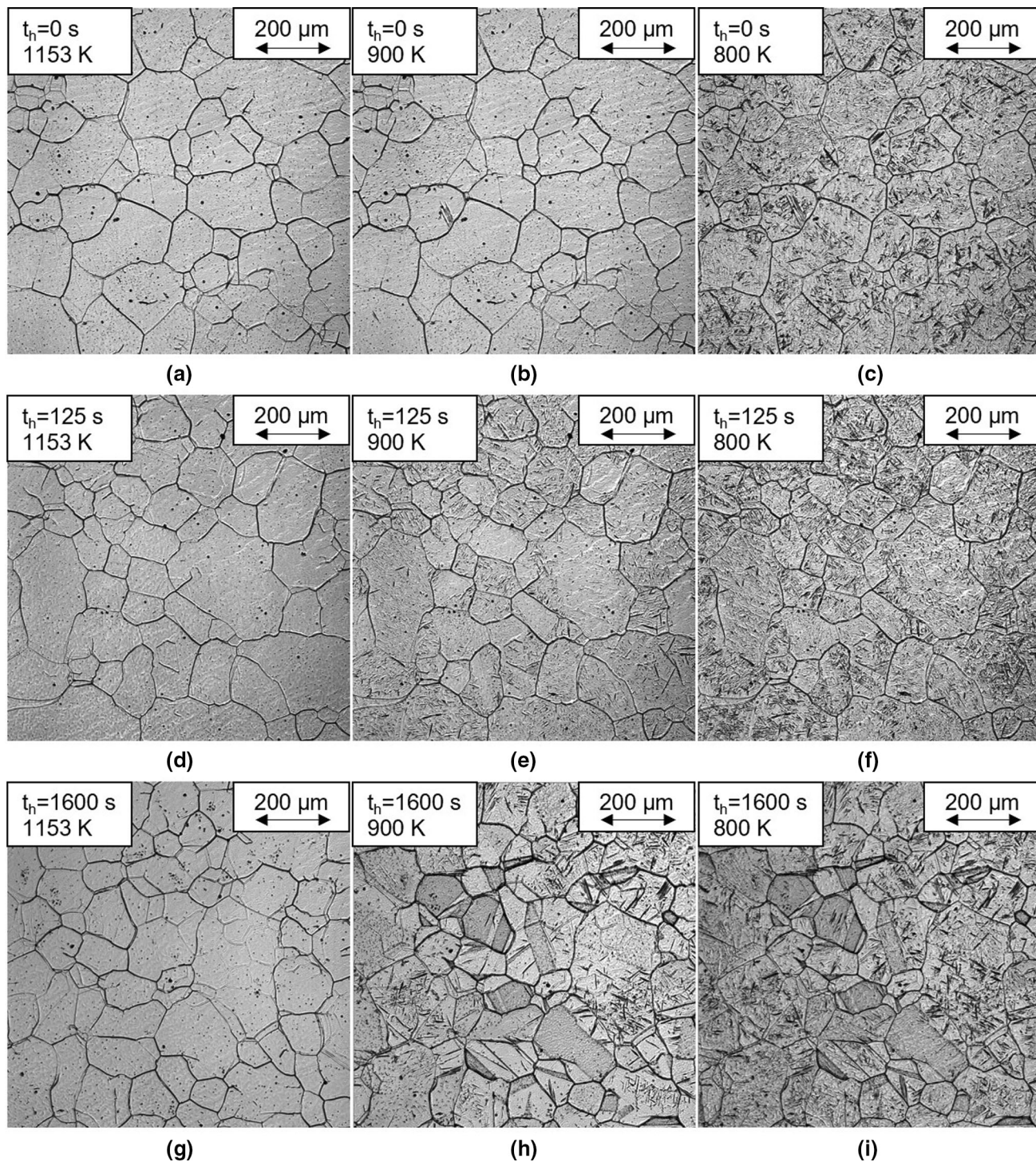


Fig. 6—HT-LSCM micrographs series of the austenite-to-ferrite phase transformation during cooling with  $7 \text{ K s}^{-1}$  after annealing at 1153 K for varying holding times. (a–c) cooling sequence after 0 seconds holding at 1153 K; (d–f) cooling sequence after 125 seconds holding at 1153 K; (g–i) cooling sequence after 1600 seconds holding at 1153 K.

dilatometry signal refers to the phase transformation to grain-boundary ferrite or intragranular ferrite. Moreover, austenite grain growth is analyzed.

Figure 6 compares the recorded microstructure evolution during cooling with  $7 \text{ K s}^{-1}$  after three different holding times ( $t_h$ ) at 1153 K. A cooling rate of

approximately  $7 \text{ K s}^{-1}$  favors the formation of acicular ferrite in low-carbon microalloyed steels.<sup>[14]</sup> Figures 6(b), (e), and (h) show the effect of the varied holding at 1153 K on the acicular ferrite nucleation at 900 K, where, at prolonged holding, AF nucleation starts at higher temperatures.

The various holding times at 1553 K have a negligible impact on the prior austenite grain size (PAGS), as shown in Figure 7. Coarsening of the austenite grains is virtually completed after annealing at 1553 K.

Figure 8 depicts the final microstructure of the HT-LSCM samples after cooling to room temperature after the different studied holding times. Figures 8(a) and (c) both show a strong ferrite-decoration of former austenite grains. This effect is less pronounced at 125 seconds holding, Figure 8(b), which suggests that it should be possible to find a holding time at which grain-boundary allotriomorphs are totally absent.

*c. Comparative discussion of dilatometry and laser confocal results* Comparing the austenite-to-ferrite transition temperatures from the dilatometer to the values determined by HT-LSCM, it can be stated that the transformation temperature using the dilatometer corresponds to the starting temperature of intragranular acicular ferrite (Figure 9). Only minor amounts of grain-boundary ferrite formed, and the transformation is dominated by the intragranular formation of ferrite. The lowest formation temperature of acicular ferrite is reached at the experiments without intermediate holding at 1553 K. The low temperature goes along with the fact that no sufficient amounts of (Ti,Nb,V)(C,N) carbonitrides, which could serve as potential nucleation sites for intragranular ferrite, are yet precipitated. After 125 seconds holding, MX particles are given additional time to form and the transition temperature for ferrite rises. The highest austenite-to-ferrite transformation temperature

is reached after 1600 seconds as more and more favorable particles for the on-surface nucleation of ferrite are present.

The acicular ferrite phase fraction shows moderate dependence on the holding time, see Figure 9. The minimum phase fraction, reached with 125 seconds holding, coincides with a rather fine final microstructure, see Figure 8(b). The maximum difference of < 3 pct comparing the AF phase fractions, as derived from the heat treatments with varying intermediate holding times, lies upon the expected measurement error. Therefore, the deviations are negligible, and the intermediate holding time has to impact on the final acicular ferrite phase fraction.

## 2. Precipitate analysis from Gleeble® experiments, characterized with SEM and TEM

We now focus on the deeper understanding of the MX precipitation trends during different treatments in order to understand their role on the ferrite evolution and, thus, grain refinement. The formation of microalloy carbonitrides after varied holding at a respective test temperature is investigated by electron microscopy.

*a. Precipitate distribution* After examining the quenched compression test samples in TEM, the average number density and sizes of precipitates are determined with the software ImageJ. Figure 10 depicts the detected particles of the compressed as well as not deformed materials with different holding times analyzed via STEM-HAADF.

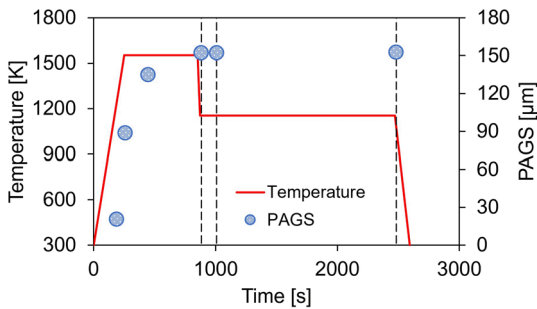


Fig. 7—Evolution of the austenite grain size during thermal treatment using HT-LSCM. The vertical auxiliary lines indicate the different holding times.

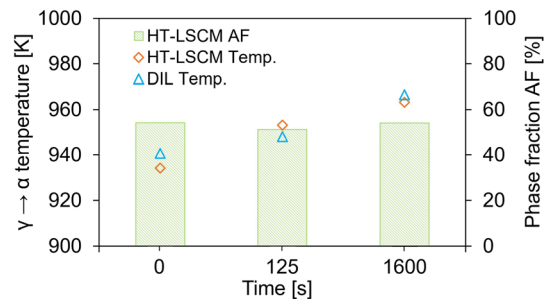


Fig. 9—Comparison of austenite-to-ferrite transformation temperatures as obtained from dilatometer/HT-LSCM and acicular ferrite phase fraction after quenching of HT-LSCM samples for varying intermediate holding times (0–1600 seconds) at 1553 K.

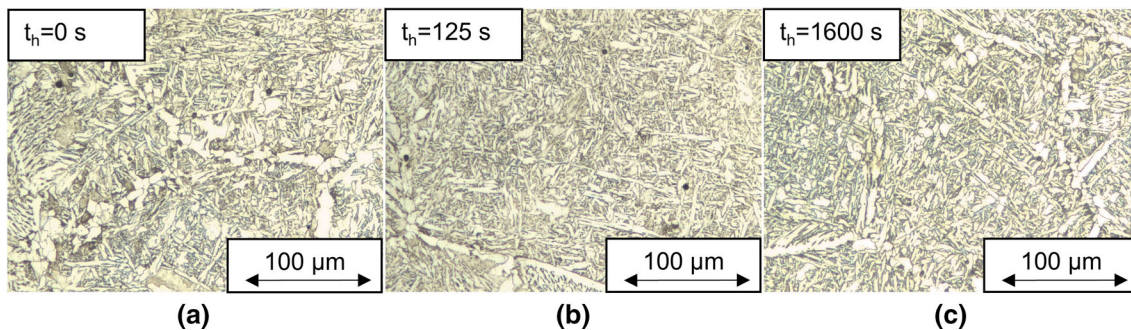


Fig. 8—Light microscopy images of HT-LSCM samples after cooling with  $7 \text{ K s}^{-1}$  to room temperature. (a) 0 seconds holding at 1153 K; (b) 125 seconds holding at 1153 K; (c) 1600 seconds holding at 1153 K.

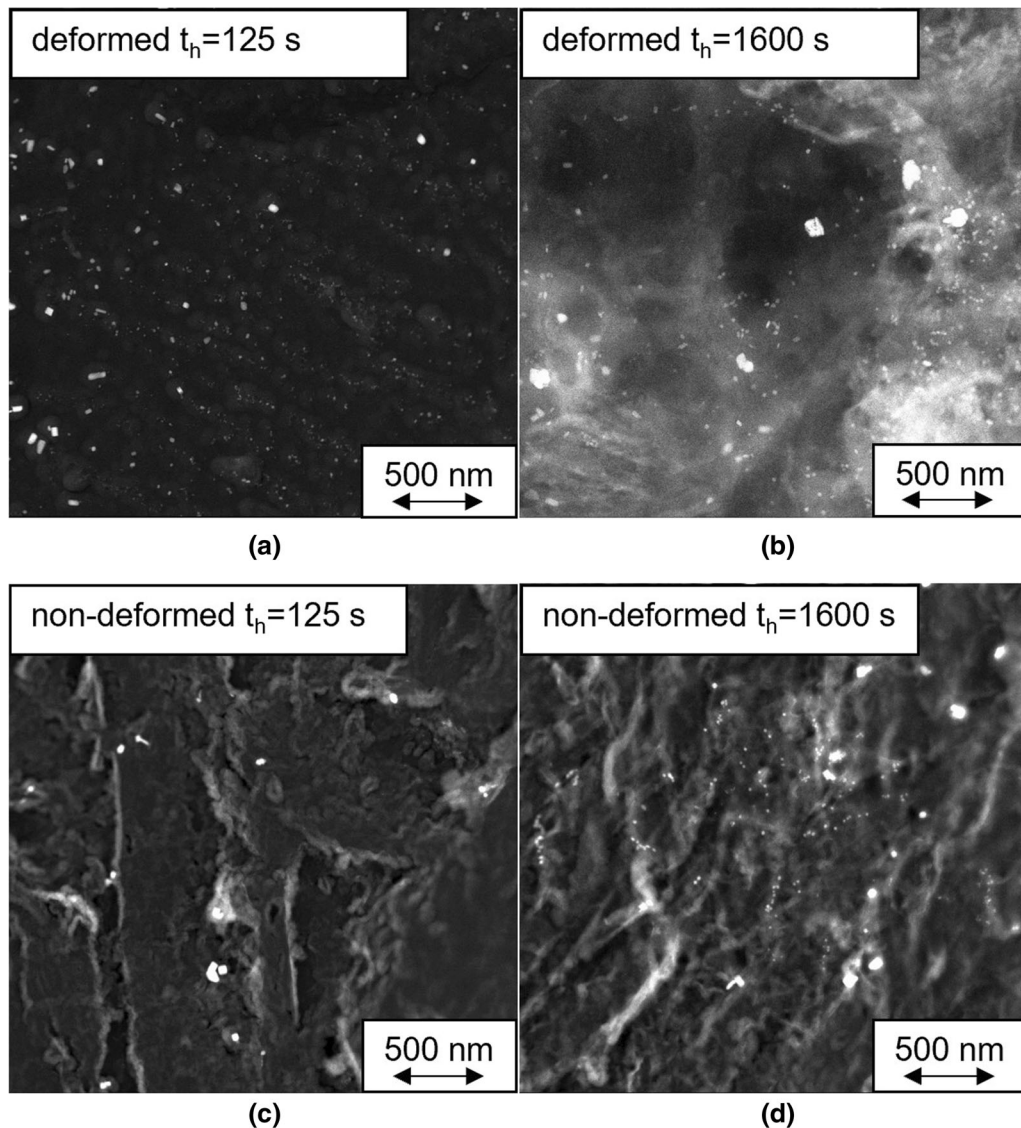


Fig. 10—STEM-HAADF images of replicas after quenching to room temperature; Gleeble® heat treatments with varying holding times at 1553 K. (a) Deformed, 125 seconds holding; (b) deformed, 1600 seconds holding; (c) non-deformed, 125 seconds holding; (d) non-deformed, 1600 seconds holding.

Figure 11 illustrates the size distribution of the detected particles. Our findings show that the amount of MX serving as potential nucleation sites for intragranular ferrite slightly increases at prolonged holding. Deformation enhances the formation of finely dispersed precipitates. The number-weighted mean radii have to be considered with caution due to the determined bimodal distribution.

It should be noted that only a small volume of the material can be analyzed in TEM, and a large number of samples would be needed for statistical accuracy of the precipitate distribution. Replicas of the material are used for the analysis of the precipitates. This can result in slight deviations since all particles extracted from the matrix are included in the number density and size evaluation, and no distinction between carbonitrides and other phases is made.

The bright carbon film leads to possible difficulties in the evaluation by contrast analysis.

While the evaluated average mean radius can be used as a reliable reference, a precise statement of the experimental phase fractions and particle number densities is delicate because of the small inspected microstructure section and comparatively poor statistics. In this work, three images are used for the examination of each individual material condition, respectively. Therefore, TEM is particularly used to obtain an overall view of the average nano-particle sizes and the evaluation of phases below the detection limits of SEM analysis.

*b. MX chemistry and nucleation sites of phases* The chemical composition of the detected phases is analyzed by TEM- and SEM-EDX mappings. The cube-like

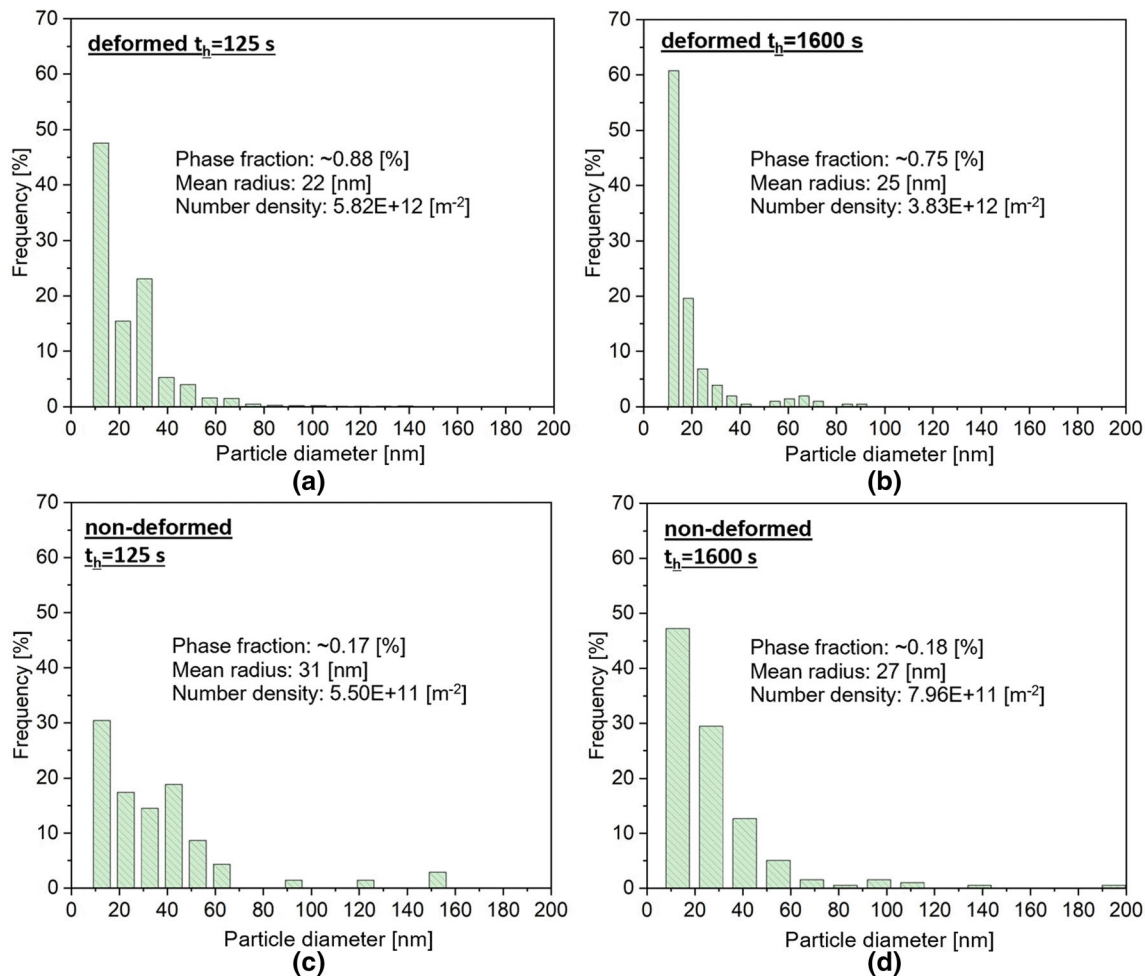


Fig. 11—Size distribution of precipitates in the matrix. STEM particle analysis with ImageJ after Gleeble® compression tests (a, b) and heat treatments (c, d) with varying holding times at 1553 K. Average relative phase fraction, mean radius, and number density are inserted.

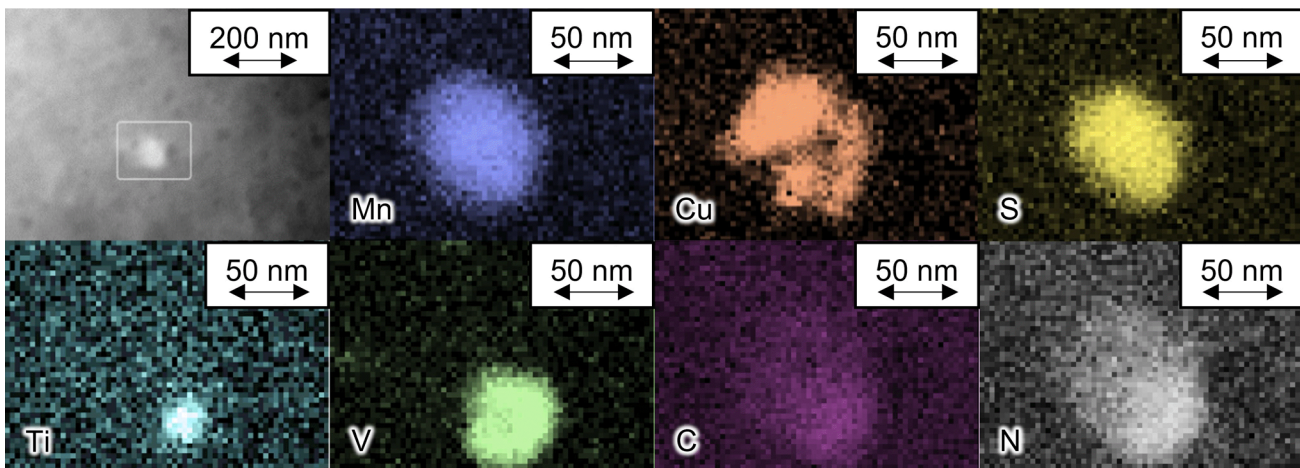


Fig. 12—TEM-EDX mapping of thin film sample after compression test from Gleeble® with 125 seconds holding time.

precipitates in Figure 10 are MX phases, while spherical particles are identified as (Mn,Cu)S. To determine the chemical composition of the finely dispersed particles of Figures 10(b) and (d), EFTEM images are employed. The analysis shows that the larger precipitates are

mostly (Ti,V)(C,N) phases, while the smaller precipitates (< 50 nm) predominantly contain only vanadium.

Figures 12 and 13 show typical complex mixed carbonitrides, where MX particles form on pre-existing (Mn,Cu)S particles. In Figure 13, the analysis of C is

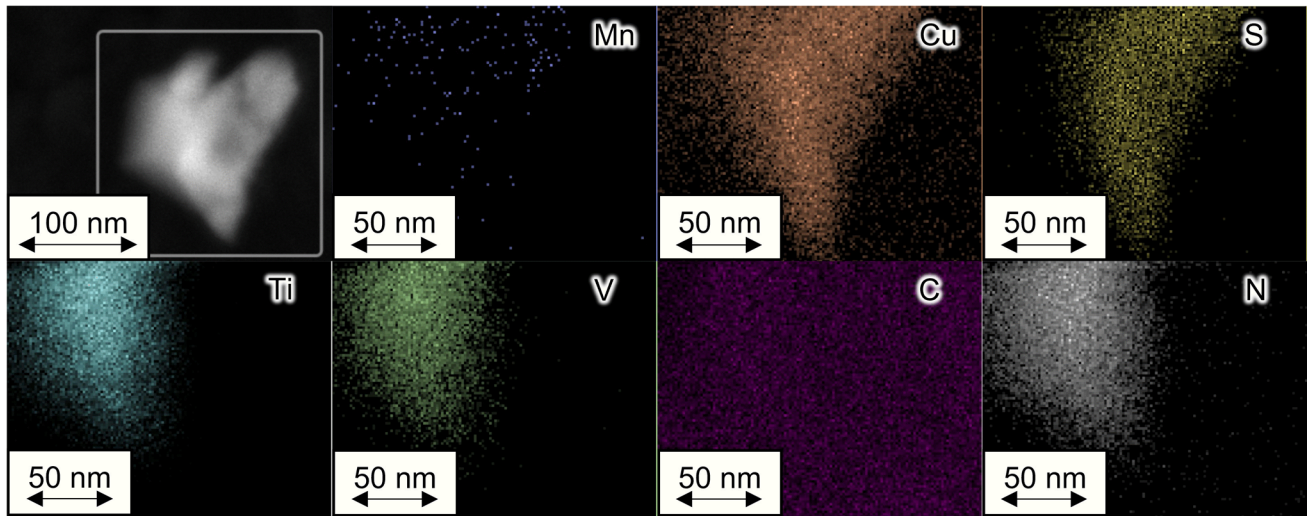


Fig. 13—TEM-EDX mapping of replica sample after heat treatment from Gleeble® with 125 seconds holding time.

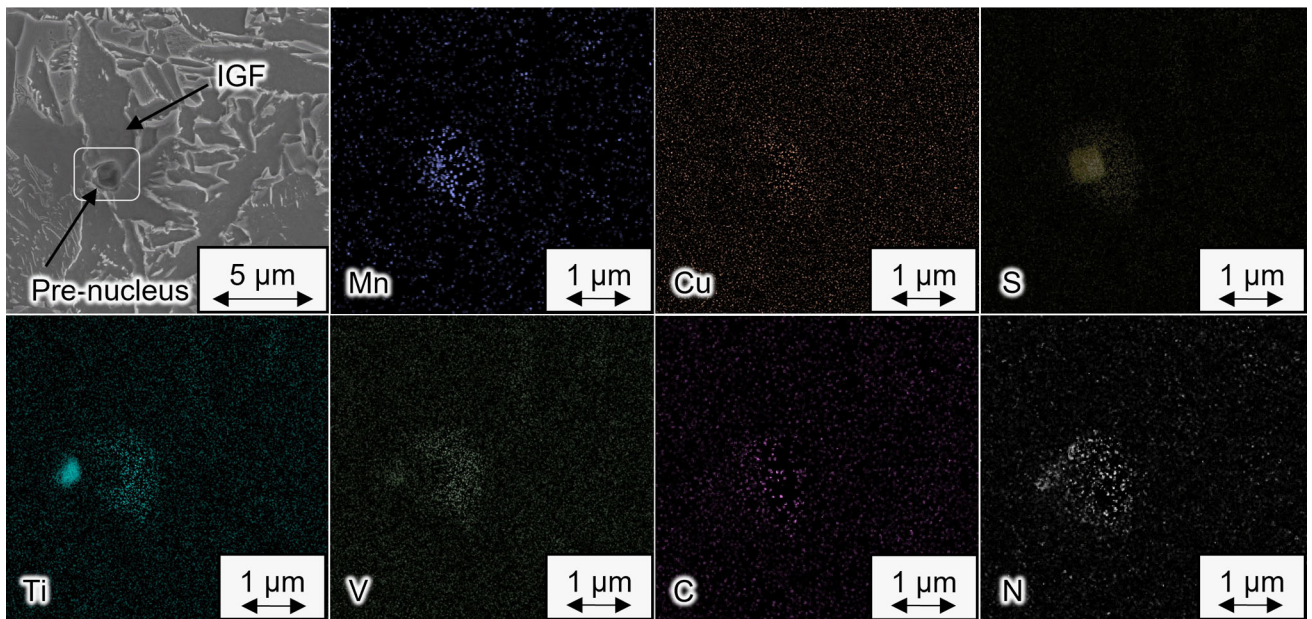


Fig. 14—SEM-EDX mapping of thin film sample after thermal treatment from Gleeble® with 25 seconds holding time.

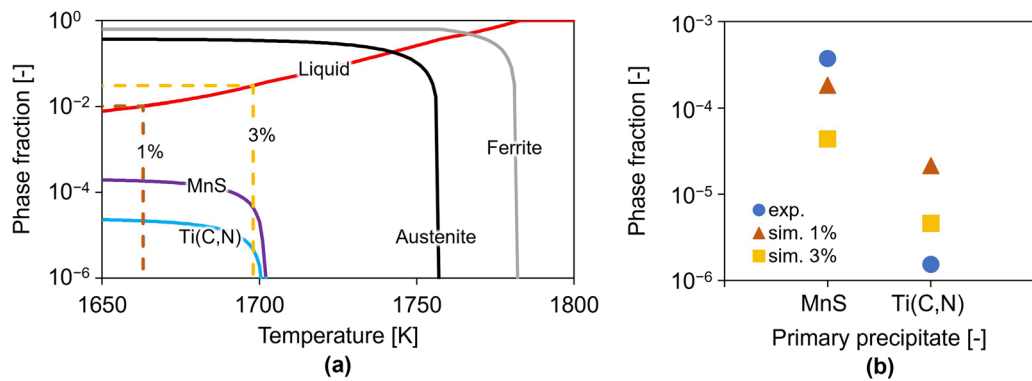


Fig. 15—Scheil-Gulliver calculation. (a) Phase fractions of examined microalloyed steel grade at 1 and 3 pct residual liquid; (b) Comparison of MnS and Ti(C,N) phase fractions from simulation and SEM-EDX analysis.

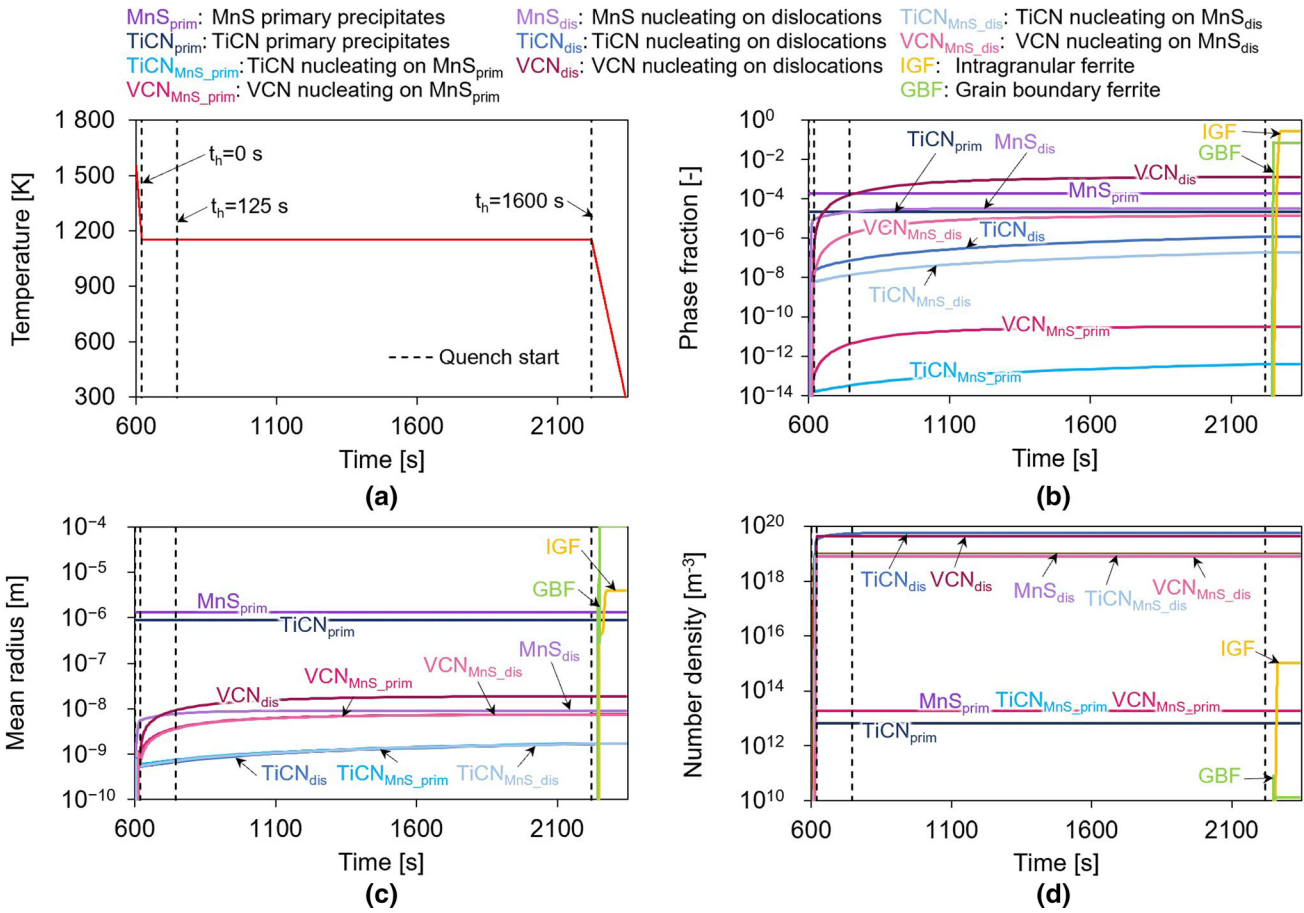


Fig. 16—Simulation of MX precipitation and intragranular ferrite formation during thermal treatments with various holding times at 1153 K. (a) Schematic treatment; (b) Phase fractions; (c) Mean radii; (d) Number densities.

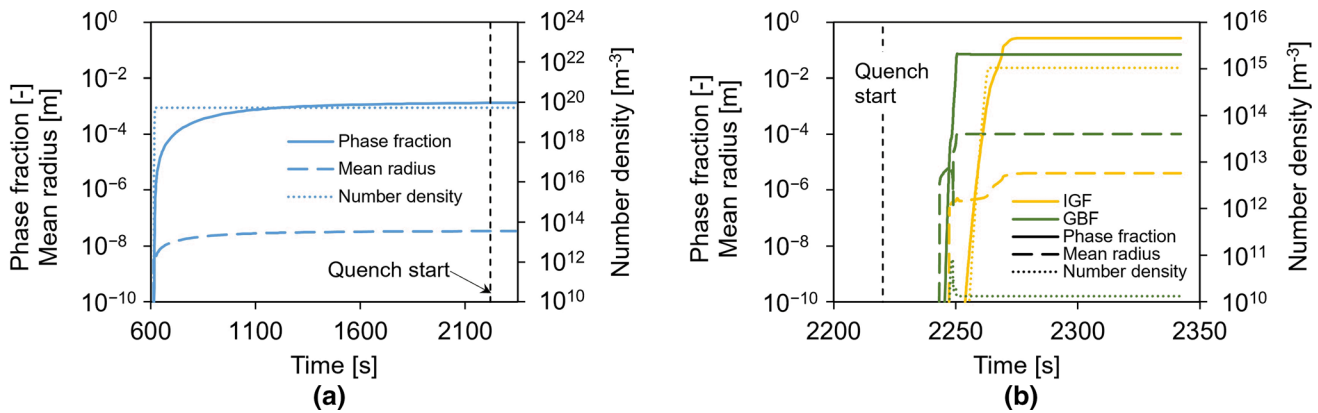


Fig. 17—Close-up of phase fraction, mean radius, and number density of phases during simulation of thermal treatment with 1600 seconds holding at 1153 K. (a) V(C,N); (b) IGF and GBF.

impeded by the carbon film of the replica and, therefore, the detection of C is not feasible. Figure 14 depicts acicular ferrite formation on a (Mn,Cu)S + (Ti,V)(C,N) particle. More precisely, the image shows the AF nucleation on a (Ti,V)(C,N), which formed on a primary (Mn,Cu)S particle.

## B. Simulation

### 1. Simulated primary precipitates

The simulative determination of primary precipitates is necessary for the realistic computation of thermomechanical processes, as primaries partially consume individual elements, and the respective element fraction

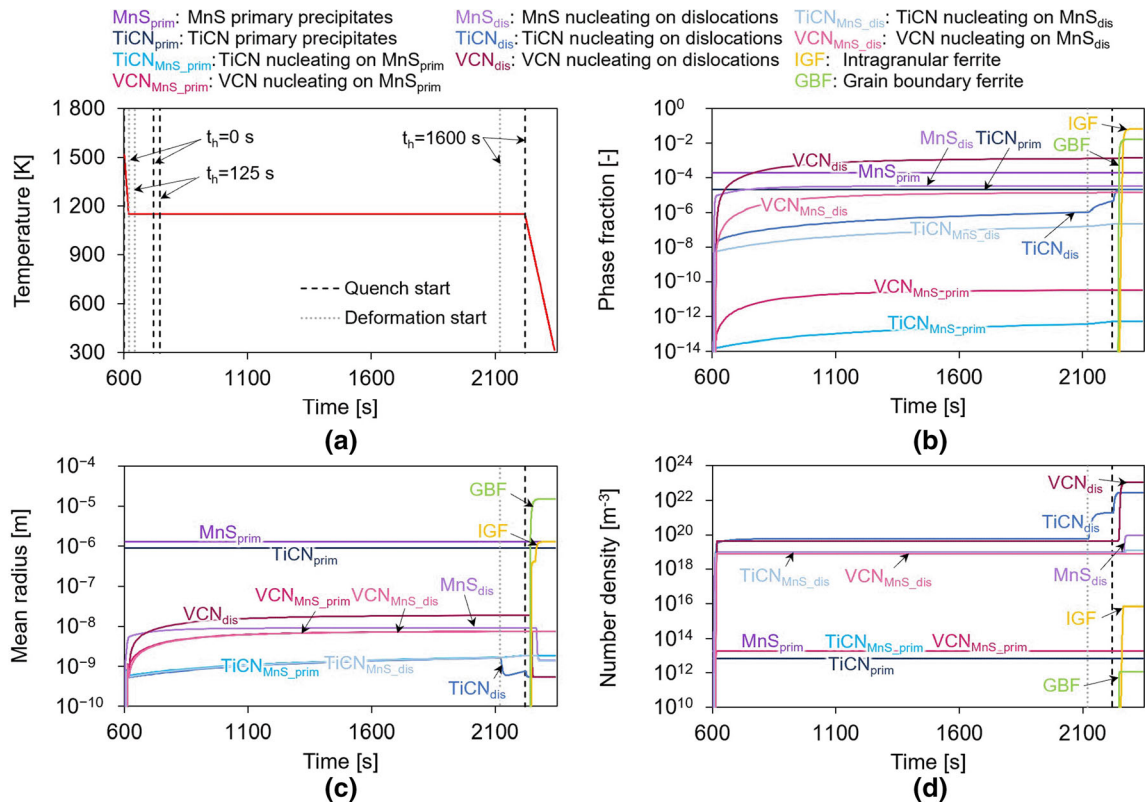


Fig. 18—Simulation of MX precipitation and intragranular ferrite formation during compression tests with various holding times at 1153 K. (a) Schematic treatment; (b) Phase fractions; (c) Mean radii; (d) Number densities.

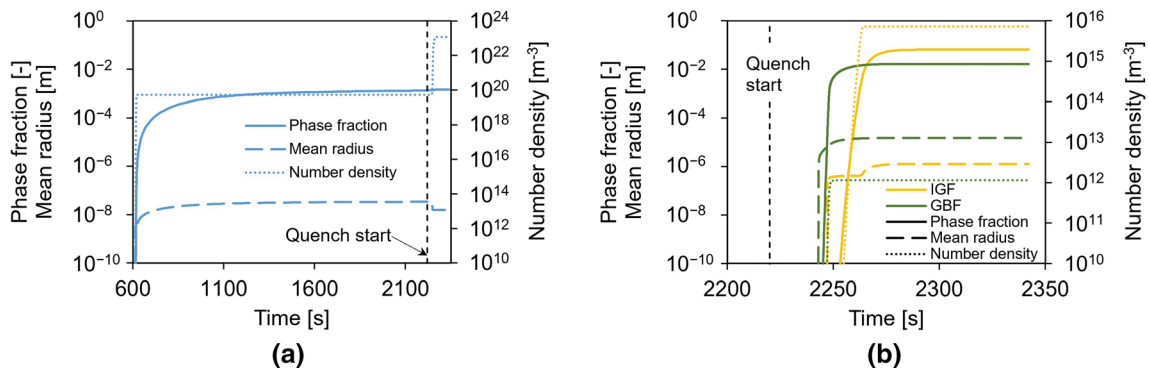


Fig. 19—Close-up of phase fraction, mean radius, and number density of phases during simulation of compression test with 1600 seconds holding at 1153 K. (a) V(C,N); (b) IGF and GBF.

is not available for subsequent secondary precipitation. Using the Scheil–Gulliver method<sup>[70–72]</sup> with back-diffusion of the light interstitial elements C and N, the primary phases of the examined microalloyed steel are predicted and compared to the results of the experimental analyses.

Figure 15(a) shows the Scheil–Gulliver simulation with 3 and 1 pct residual liquid phase limits, respectively. Primary phases are expected to nucleate in the residual liquid of the solidifying matrix. The different fractions of the remaining liquid correspond to the applied cooling rates. A value of 3 pct is used for fast quenching, while a lower value of 1 pct is applied for

slow cooling rates. Our results show that MnS and Ti(C,N) are expected to precipitate from the melt in both instances.

Figure 15(b) compares the Mn-sulfide and Ti-carbonitride phase fractions from simulation with the experimental data of the as-cast base material without any additional thermomechanical treatment. Since V(C,N) has a high solubility in the austenite phase,<sup>[1]</sup> it precipitates at lower temperatures and no primary V(C,N) phases are formed. The results from the calculation with 1 pct residual liquid are used for the following simulations due to the moderate experimental cooling rates. This primary precipitate modeling is

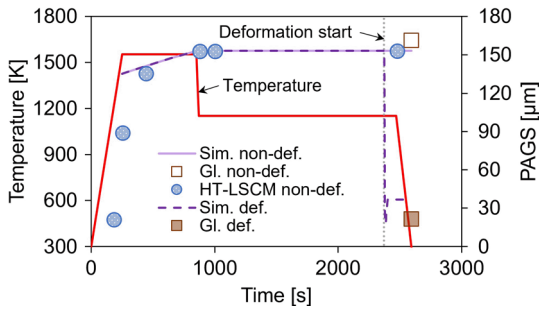


Fig. 20—Comparison of austenite grain sizes during compression tests (def.) and thermal treatments (non-def.) with 1600 seconds holding at 1153 K, simulated (Sim.), experimental Gleeble® (Gl.), and experimental HT-LSCM.

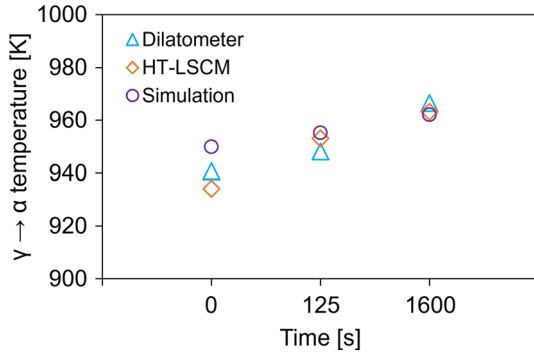


Fig. 21—Comparison of the IGF transformation temperature during thermal treatments with varied holding times at 1153 K, experimentally determined by dilatometry, HT-LSCM, and simulated.

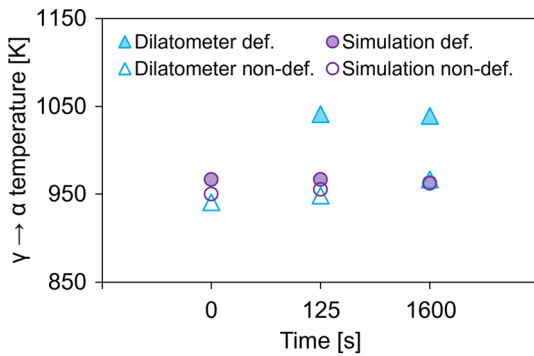


Fig. 22—Comparison of IGF transformation temperature during compression tests (def.) and thermal treatments without deformation (non-def.) with varied holding at 1153 K, experimentally determined by dilatometry and simulated.

included in the simulations to define the amount of each element available for the subsequent MX and ferrite precipitation.

## 2. Impact of MX precipitation during thermal treatments on the ferrite formation

The effect of carbonitrides on the ferrite nucleation within austenite grains is investigated *via* computational modeling. For the formation of MX phases and intragranular ferrite on already existing particles, the

on-particle nucleation model is applied. The thermal treatment of Figure 1 without deformation is used. Figure 16 depicts the simulation results for various holding times. The first black-dotted vertical auxiliary line on the left-hand side of the plots marks the start of holding at 1153 K, while the second and third one indicate 125 seconds and 1600 seconds at the test temperature. The formation of IGF and GBF in Figure 16 corresponds to the treatment with 1600 seconds intermediate holding.

The phase fractions and the mean radii of MX phases, formed at dislocations and on primary MnS, increase at longer holding times while the number densities remain unchanged. Figure 17(a) summarizes the precipitate evolution of all V(C,N) phases, representing potential nucleation sites for intragranular ferrite. The carbonitride phases grow, but no coarsening occurs. This is indicated by the number of precipitates, which stays the same.

After holding for 1600 seconds at 1153 K and cooling with  $7 \text{ K s}^{-1}$ , intragranular ferrite reaches approximately 27 pct of all phases at room temperature, Figure 17(b). The final microstructure contains about 7 pct of grain-boundary ferrite. These computational observations are in good accordance with the light microscopy images, Figures 5(d) and 8(c), as intragranular formed acicular ferrite predominates besides grain-boundary ferrite and pearlite.

## 3. Impact of strain-induced MX precipitation on ferrite formation

The formation of intragranular ferrite on deformation-induced microalloy carbonitrides is computed in a thermomechanical simulation equal to the schematic treatment of Figure 1. Annealing at 1553 K for 600 seconds is followed by cooling to 1153 K. After holding for 0, 25, or 1500 seconds, respectively, a deformation step of  $0.01 \text{ s}^{-1}$  to a true strain of 1 is considered, Figure 18(a). Figure 18(b) through (d) gives an insight into the precipitation during the compression tests with 1500 seconds holding before deformation for 100 seconds. It should be mentioned that there is no difference concerning the heat treatments of Figures 16 and 18. The compression test only involves an additional deformation after 1500 seconds holding at the test temperature. Therefore, the simulation of MX precipitation and intragranular ferrite formation during the compression tests shows the same results as compared to the thermal treatment until the deformation starts.

Figure 19(a) illustrates the precipitate evolution of V(C,N) during the compression test with 1500 seconds holding before the deformation. Similar to the results from the non-deformation experiments, phase fractions and mean radii of the secondary phases increase during holding while the number densities remain the same. During deformation, the number of dislocations acting as nucleation sites rises and the number density of the precipitates increases drastically during cooling.

Comparing the formation of GBF from the thermal treatments (Figure 17(b)) to that during the deformation tests (Figure 19(b)) shows that the number density of GBF values increases. This is caused by the austenite



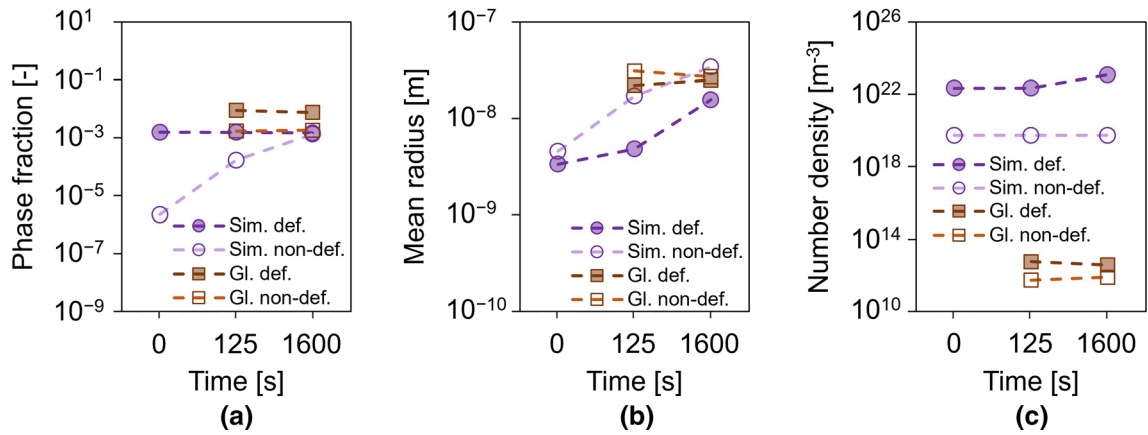


Fig. 23—Final phase fractions (a), mean radii (b), and number densities (c) of the sum of all V(C,N) phases from simulation (Sim.) as well as of experimental STEM particle analysis of Gleeble® samples (Gl.) from compression tests (def.) and thermal treatments (non-def.) with various holding times at 1153 K. The dashed lines are an aid to help the reader's eye follow the trend.

grain evolution, as the prior austenite grains are expected to be smaller after compression (see Section III.C.1) due to deformation-induced recrystallization. Therefore, the higher amount of grain boundaries leads to more potential nucleation sites for GBF. Additionally, the dislocation density rises during deformation, which leads to a higher number of nucleation sites for MX phases and ferrite than in the experiments without deformation.

As the deformation simulations in this study focus on the intragranular nucleation of ferrite on carbonitrides, and no formation of ferrite on dislocations<sup>[76,77]</sup> is considered, the ferrite phase fraction of the experimentally investigated microstructure (Figure 5(b)) is expected to be higher than the simulation results.

### C. Comparison of PAGES, IGF Transformation Temperatures, and Precipitate Evolution from Experiments and Simulation

#### 1. Austenite grain size

A comparison of the austenite grain sizes indicates that the grains of non-compressed samples are much larger than those of the compressed ones after the same thermal treatment due to recrystallization, Figure 20. The size of the former austenite grains directly affects the formation of intragranular ferrite, as large austenite grains promote the development of intragranular ferrite. This matches the observation that the materials which underwent deformation feature a smaller IGF phase fraction than the non-compressed samples after cooling to room temperature (Figures 17(b) and 19(b)). The simulation results of the austenite grain evolution correlate well with the experimentally determined prior austenite grain sizes from Gleeble and HT-LSCM tests.

#### 2. IGF nucleation temperature

Figure 21 compares the experimental austenite-to-ferrite transformation temperatures of the thermal treatments from dilatometer and HT-LSCM to the results from precipitation and microstructure evolution simulation. The computed transformation temperature is

determined from the simulation results of Figure 16. The temperatures correspond to the first appearance of IGF.

The increasing nucleation temperature of intragranular ferrite with prolonged holding at 1153 K from precipitation simulation correlates well with the experimentally determined values. The most significant deviation of 15 K occurs at the tests without intermediate holding (0 second). Although the simulation indicates the actual start of ferrite formation, whereas the HT-LSCM values are obtained from the visual observation of the first appearance of ferrite, this deviation is negligible.

The results of the intragranular ferrite formation temperature from simulation and dilatometer experiments with deformation, Figure 22, show a large mutual deviation, contrary to those without compression. The difference of about 75 K may be caused firstly by difficulties in the evaluation of the transformation temperature from the dilatometer tests by plotting dilatation against the temperature (Figure 4(a)). During compression tests, the dilatation is not only affected by the phase transformation but also by the deformation of the sample. Secondly, the present simulation results focus on the formation of IGF on MX particles, while the nucleation of ferrite on dislocations is excluded. Anyway, the stagnating trend of both examination variants coincides. The different holding times before the compression have a negligible impact on the transition of the phases as deformation strongly elevates the amount of potential ferrite nucleation sites.

#### 3. Carbonitride particle distribution

V(C,N) particles are analyzed in detail, as they are expected to be the most effective nucleation site for IGF. When analyzing the impact of different holding times before the compression on the final precipitate distribution after cooling to room temperature, Figure 23, the simulative phase fraction stays almost unchanged. On the other hand, the mean radius and the number density increase at the tests with longer holding prior to deformation. The results from the experiments without compression show that the particles grow to larger sizes

at a constant number density and increasing phase fraction at extended holding.

After 1600 seconds at 1153 K, V(C,N) precipitates from the non-deformation tests are, on average, twice as big as the particles from the experiments with compression, while the phase fraction is determined to remain the same. For the intragranular nucleation of ferrite, the bigger size (~ 35 nm diameter) and, therefore, the larger surface area of the particles without deformation is presumably more favorable, although the number density of the particles is lower in comparison to the MX of the compression tests. This may explain the higher amount of IGF of the non-deformation simulation after cooling to room temperature, Figure 17(b), compared to the ferrite content after the compression tests, Figure 19(b).

Figure 23 also compares the carbonitride precipitate evolution from simulation to the particle analysis from experiments. The mean radius of the examined material correlates well with the data spectrum from the simulation.

#### IV. SUMMARY AND CONCLUSION

The temperature of the austenite-to-ferrite transformation is investigated *via* dilatometry and HT-LSCM. The HT-LSCM tests confirm that the transformation temperature obtained from the dilatometer experiments actually corresponds to the formation temperature of acicular ferrite. Prolonged holding at the test temperature without deformation elevates the transformation temperature. In contrast, the compression experiments show that the austenite-to-ferrite temperature is elevated to the same high temperature, irrespective of the intermediate holding time. For complete microstructure simulation of thermomechanical treatments *including* deformation, on one hand, the formation of ferrite on dislocations has to be considered, and on the other hand, the on-particle nucleation of ferrite is assumed to be negligible.

*Without* deformation, the formation of ferrite triggered by the precipitation of MX carbonitrides in combination with the on-particle nucleation of ferrite is predicted, which indicates the important role of MX for the case of sole thermal treatments. The physical-based calibration of simulation input parameters allows for predictive modeling of precipitation and growth kinetics involving the on-particle nucleation of MX phases on primary phases and intragranular ferrite on complex mixed carbonitrides. A constrained volumetric mismatch between MX and steel matrix due to the elastically stressed matrix and precipitates at dislocations, yielding 1/10 of the full volumetric mismatch, is used. The simulated ferrite formation temperatures of the non-deformation tests are in accordance with the experimental results.

In our work, a V-rich steel grade with comparatively low additions of Ti is examined. For a general conclusive statement that the ferrite formation temperature is induced by V(C,N), a Ti-rich microalloyed steel grade with low additions of V should be investigated. This would show whether or under which conditions Ti(C,N) might serve as nucleation site for intragranular ferrite.

The microstructure and precipitation evolutions from Gleeble experiments serve as a validation base for the kinetic precipitation simulation. The computational thermodynamics of MX, together with the  $T_{crit}$  approach for the diffuse interface between MX and steel matrix as well as the calibrated inner particle diffusion factor of 0.15 for ferrite, as compared to  $\leq 0.01$  for carbonitrides, allow us to describe the formation of the present phases thoroughly within the simulations. The simulated precipitate evolution is combined with a model for the dislocation evolution with physically assessed parameters and a recrystallization model to predict the austenite grain size evolution and the on-particle nucleation of ferrite on pre-existing particles.

Both experiments and simulation show that intragranular ferrite nucleates preferably on mixed (Mn,Cu)S + (Ti,V)(C,N) carbonitride complexes. It is proposed that the increase of the ferrite formation temperature is induced by larger amounts of V(C,N) with around 35 nm diameter, serving as favorable nucleation sites for intragranular ferrite.

#### ACKNOWLEDGMENTS

The financial support from the Austrian Federal Ministry for Digital and Economic Affairs and the National Foundation for Research, Technology, and Development is gratefully acknowledged. The financial support, as well as the provision of sample material by voestalpine Tubulars GmbH & Co KG, is gratefully acknowledged by the authors. This research was funded by Christian Doppler Forschungsgesellschaft in the framework of the CD-Laboratory of Interfaces and Precipitation Engineering. The authors are thankful to the Chair of Ferrous Metallurgy at Montanuniversität Leoben for the performance of the HT-LSCM measurements. The TEM analysis was carried out using facilities at the University Service Centre for Transmission Electron Microscopy, TU Wien, Austria.

#### CONFLICT OF INTEREST

On behalf of all authors, the corresponding author states that there is no conflict of interest.

#### FUNDING

Open access funding provided by TU Wien (TUW).

#### OPEN ACCESS

This article is licensed under a Creative Commons Attribution 4.0 International License, which permits use, sharing, adaptation, distribution and reproduction

in any medium or format, as long as you give appropriate credit to the original author(s) and the source, provide a link to the Creative Commons licence, and indicate if changes were made. The images or other third party material in this article are included in the article's Creative Commons licence, unless indicated otherwise in a credit line to the material. If material is not included in the article's Creative Commons licence and your intended use is not permitted by statutory regulation or exceeds the permitted use, you will need to obtain permission directly from the copyright holder. To view a copy of this licence, visit <http://creativecommons.org/licenses/by/4.0/>.

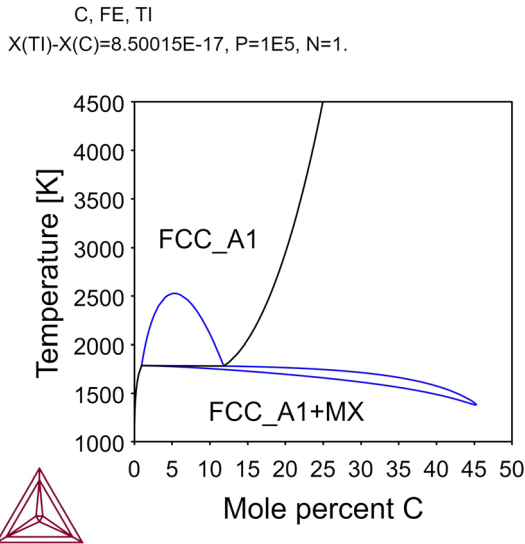


Fig. A1—Phase diagram Fe–TiC.

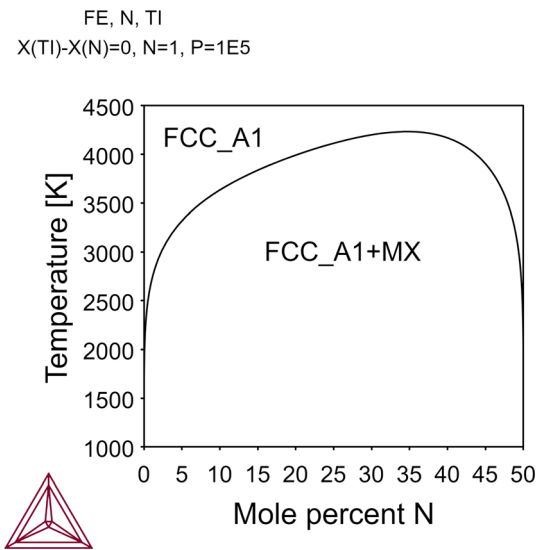


Fig. A2—Phase diagram Fe–TiN.

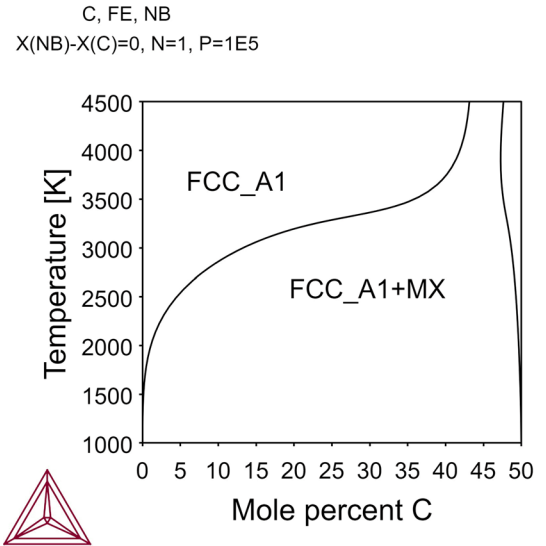


Fig. A3—Phase diagram Fe–NbC.

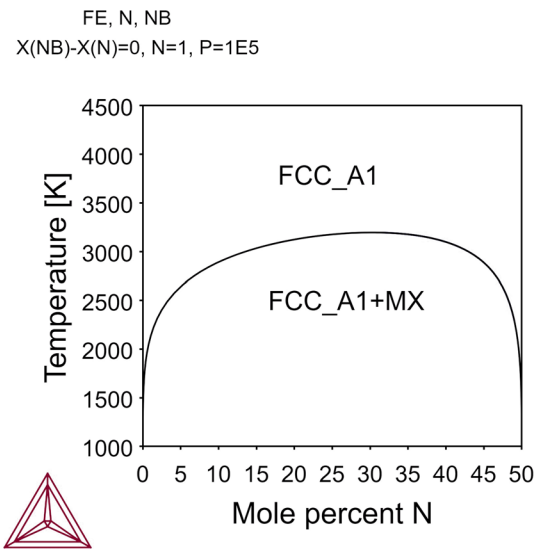


Fig. A4—Phase diagram Fe–NbN.

## APPENDIX

As a consequence of the complex and questionable demixing behavior of TiC, it is impossible to determine a  $T_{crit}$ , Figure A1. The critical temperature of NbC, Figure A3, is only estimated as the miscibility gap is not entirely closed. The miscibility gap of VN, Figure A6, shows a nonuniform progression. The  $T_{crit}$  is, therefore, approximated.

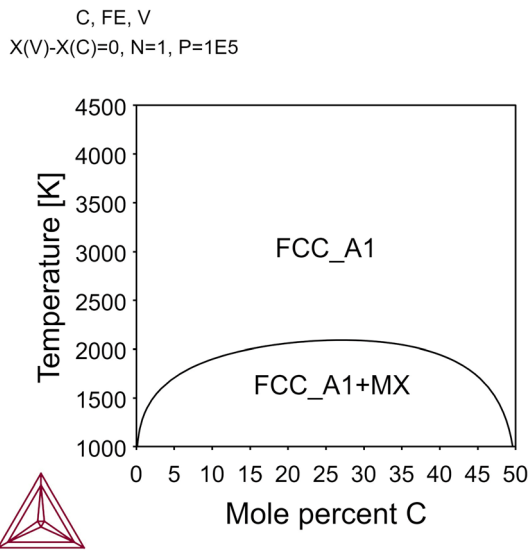


Fig. A5—Phase diagram Fe-VC.

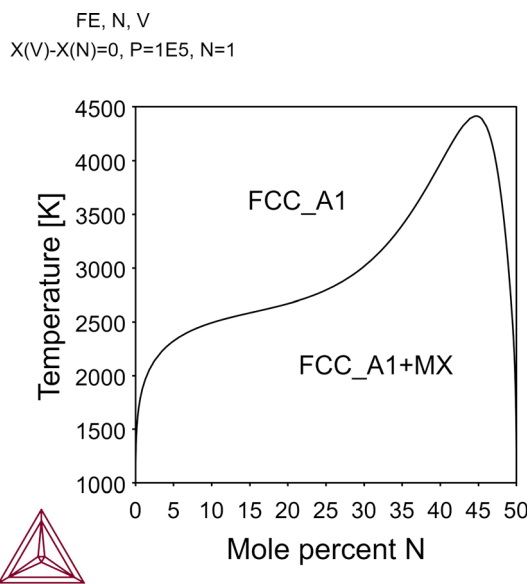


Fig. A6—Phase diagram Fe-VN.

## REFERENCES

1. T. Gladman: *The Physical Metallurgy of Microalloyed Steels*, 1st ed. Maney Publishing, London, 1997.
2. T.N. Baker: *Ironmak. Steelmak.*, 2016, vol. 43, pp. 264–307.
3. R. Lagneborg, B. Hutchinson, T. Siwecki, and S. Zajac: *The Role of Vanadium in Microalloyed Steels*, 1st ed. Swerea KIMAB, Kista, 2014.
4. S. Zajac, B. Hutchinson, R. Lagneborg, and M. Korchynsky: *la metallurgia italiana*, 2009, vol. 101, p. 39–48.
5. P. Tao, X. Chai, J. Wang, S.U. Hang, and C. Yang: *J. Iron Steel Res. Int.*, 2015, vol. 22, pp. 1037–042.
6. A. Karmakar, S. Biswas, S. Mukherjee, D. Chakrabarti, and V. Kumar: *Mater. Sci. Eng. A*, 2017, vol. 690, pp. 158–69.
7. A.M. Elwaziry, E. Essadiqi, and S. Yue: *ISIJ Int.*, 2004, vol. 44, pp. 162–70.
8. C. Zhou and R. Priestner: *ISIJ Int.*, 1996, vol. 36, pp. 1397–405.
9. B. Dutta, E. Valdes, and C.M. Sellars: *Acta Metall. Mater.*, 1992, vol. 40, pp. 653–62.

10. T. Furuhashi, J. Yamaguchi, N. Sugita, G. Miyamoto, and T. Maki: *ISIJ Int.*, 2003, vol. 43, pp. 1630–639.
11. T.N. Baker: *Ironmak. Steelmak.*, 2017, vol. 46, pp. 1–55.
12. D. Loder, S.K. Michelic, and C. Bernhard: *J. Mater. Sci. Res.*, 2017, vol. 6, pp. 24–43.
13. E. Gamsjäger, F.D. Fischer, and J. Svoboda: *Mater. Sci. Eng. A*, 2004, vol. 365, pp. 291–97.
14. S.K. Michelic, D. Loder, G. Arth, and C. Bernhard: *MSF*, 2014, vol. 783–786, pp. 1079–084.
15. D. Loder, S.K. Michelic, and C. Bernhard: *Fortschritte in der Metallographie*, 2014, vol. 46, pp. 125–30.
16. C. Capdevila, F.G. Caballero, C. García Mateo, and C.G. de Andrés: *Mater. Trans.*, 2004, vol. 45, pp. 2678–85.
17. M. Enomoto: *Met. Mater. Int.*, 1998, vol. 4, pp. 115–23.
18. S.F. Medina, L. Rancel, M. Gómez, R. Ishak, and M. de Sanctis: *ISIJ Int.*, 2008, vol. 48, pp. 1603–608.
19. K.M. Wu, Y. Inagawa, and M. Enomoto: *Mater. Charact.*, 2004, vol. 52, pp. 121–27.
20. D.S. Sarma, A.V. Karasev, and P.G. Jönsson: *ISIJ Int.*, 2009, vol. 49, pp. 1063–074.
21. H.K.D.H. Bhadeshia: *Bainite in Steels: Transformations, Microstructure and Properties*, 3rd ed. CRC Press, London, 2004.
22. K.-T. Park, S.W. Hwang, J.H. Ji, and C.H. Lee: *Met. Mater. Int.*, 2011, vol. 17, pp. 349–56.
23. G. Miyamoto, T. Shinyoshi, J. Yamaguchi, T. Furuhashi, T. Maki, and R. Uemori: *Scr. Mater.*, 2003, vol. 48, pp. 371–77.
24. S. Nambu, Y. Takizawa, M. Ojima, J. Inoue, and T. Koseki: *ISIJ Int.*, 2017, vol. 57, pp. 1246–251.
25. D. Loder, S.K. Michelic, A. Mayerhofer, and C. Bernhard: *Metall. Mater. Trans. B*, 2017, vol. 48B, pp. 1992–2006.
26. F. Ishikawa, T. Takahashi, and T. Ochi: *Metall. Mater. Trans. A*, 1994, vol. 25A, pp. 929–36.
27. T. Furuhashi, T. Shinyoshi, G. Miyamoto, J. Yamaguchi, N. Sugita, N. Kimura, N. Takemura, and T. Maki: *ISIJ Int.*, 2003, vol. 43, pp. 2028–037.
28. S. Zajac, S.F. Medina, V. Schwinn, A. Osta, M. De Sanctis, and G. Herman: *Grain Refinement by Intragranular Ferrite Nucleation on Precipitates in Microalloyed Steels*, 1st ed. Office for Official Publications of the European Communities, Luxembourg, 2007.
29. C.G. de Andrés, F.G. Caballero, C. Capdevila, and D. San Martín: *Mater. Charact.*, 2002, vol. 49, pp. 121–27.
30. A.K. Giunelli, M. Militzer, and E.B. Hawbolt: *ISIJ Int.*, 1999, vol. 39, pp. 271–80.
31. N. Fuchs and C. Bernhard: *Mater. Today Commun.*, 2021, vol. 28, p. 102468.
32. DIN Deutsches Institut für Normung e. V., *Stahl – Mikrophotographische Bestimmung der erkennbaren Korngröße*, 77.040.99, EN ISO 643:2020, 2020.
33. M. Beckert and H. Klemm: *Handbuch der metallographischen Ätzverfahren*, 1st ed. VEB Deutscher Verlag für Grundstoffindustrie, Leipzig, 1966.
34. M.F. Ashby and R. Ebeling: *AIME Met. Soc. Trans.*, 1966, vol. 236, pp. 1396–404.
35. ImageJ (W. Rasband), <https://imagej.nih.gov/ij/index.html>.
36. Thermodynamic database with modified carbo-nitride descriptions based on the open-license multi-component MatCalc database mc\_fe, version 2.060 (CDL-IPE, Institute of Materials Science and Technology, TU Wien, Vienna, 2023), [https://www.matcalc.at/images/stories/Download/Database/mc\\_fe\\_v2.060.tdb](https://www.matcalc.at/images/stories/Download/Database/mc_fe_v2.060.tdb). Accessed 4 Apr 2023.
37. Open-license multi-component MatCalc diffusion mobilities database mc\_fe version 2.012 (Institute of Materials Science and Technology, TU Wien, Vienna, 2023), [https://www.matcalc.at/images/stories/Download/Database/mc\\_fe\\_v2.012.ddb](https://www.matcalc.at/images/stories/Download/Database/mc_fe_v2.012.ddb). Accessed 4 Apr 2023.
38. J.E. Bailey and P.B. Hirsch: *Proc. R. Soc. A*, 1962, vol. 267, pp. 11–30.
39. S.S. Hansen, J.B. Vander Sande, and M. Cohen: *Met. Trans. A*, 1980, vol. 11, pp. 387–402.
40. J. Kreyca: *State Parameter Based Modelling of Stress-Strain Curves in Aluminium Alloys*. Dissertation, Wien, Austria, 2017.
41. H. Buken and E. Kozeschnik: *Metall. Mater. Trans. A*, 2021, vol. 52A, pp. 544–52.
42. H. Buken and E. Kozeschnik: *Metall. Mater. Trans. A*, 2017, vol. 48A, pp. 2812–818.

43. H. Buken, P. Sherstnev, and E. Kozeschnik: *Model. Simul. Mater. Sci. Eng.*, 2016, vol. 24, p. 35006.
44. H. Buken and E. Kozeschnik: *Conf. Ser.: Mater. Sci. Eng.*, 2015, vol. 119, p. 12023.
45. H. Buken, S. Zamberger, and E. Kozeschnik: *Proceedings of the 6th International Conference on Recrystallization and Grain Growth*, 2016, pp. 113–18.
46. K.C. Russell: *Adv. Colloid Interface Sci.*, 1980, vol. 13, pp. 205–318.
47. J. Svoboda, F.D. Fischer, P. Fratzl, and E. Kozeschnik: *Mater. Sci. Eng. A*, 2004, vol. 385, pp. 166–75.
48. K.G.F. Janssens, D. Raabe, E. Kozeschnik, M.A. Miodownik, and B. Nestler: *Computational Materials Engineering: an Introduction to Microstructure Evolution*, Academic Press, Cambridge, 2010.
49. F.D. Fischer, J. Svoboda, E. Gamsjäger, E. Kozeschnik, and B. Sonderegger: *MRS Online Proc. Libr.*, 2006, vol. 979, pp. 0979–HH11–04.
50. R. Radis and E. Kozeschnik: *Model. Simul. Mater. Sci. Eng.*, 2010, vol. 18, p. 55003.
51. R. Radis: *Numerical Simulation of the Precipitation Kinetics of Nitrides and Carbides in Microalloyed Steel*. Dissertation, Graz, Austria, 2010.
52. F. Perrard, A. Deschamps, and P. Maugis: *Acta Mater.*, 2007, vol. 55, pp. 1255–266.
53. A.J. DeArdo: *Niobium Science and Technology: Proceedings of the Niobium 2001 International Symposium*, 2001, pp. 427–500.
54. R. Radis and E. Kozeschnik: *Model. Simul. Mater. Sci. Eng.*, 2012, vol. 20, p. 55010.
55. K. Frisk, J. Zackrisson, B. Jansson, and A. Markström: *Z. Metallkd.*, 2004, vol. 95, pp. 987–92.
56. C. Kicking: *Thermal Expansion of Sputter-Deposited Ti(C,N) Determined by High Temperature X-ray Diffraction*. Master Thesis, Leoben, Austria, 2018.
57. R.O. Elliott and C.P. Kempster: *J. Phys. Chem.*, 1958, vol. 62, pp. 630–31.
58. P. Maugis and M. Gouné: *Acta Mater.*, 2005, vol. 53, pp. 3359–367.
59. X.-G. Lu, M. Selleby, and B. Sundman: *Calphad*, 2005, vol. 29, pp. 68–89.
60. J. Ruge and H. Wohlfahrt: *Technologie der Werkstoffe*, Springer, Wiesbaden, 2013.
61. H. Zou and J.S. Kirkaldy: *Met. Trans. A*, 1991, vol. 22, pp. 1511–524.
62. B. Sonderegger and E. Kozeschnik: *Metall. Mater. Trans. A*, 2010, vol. 41A, pp. 3262–269.
63. G. Stechauner and E. Kozeschnik: *Acta Mater.*, 2015, vol. 100, pp. 135–46.
64. TCFE7 (Thermo-Calc Software), [https://www.thermocalc.com/media/10306/tcfe7\\_extended\\_info\\_2013-02-07.pdf](https://www.thermocalc.com/media/10306/tcfe7_extended_info_2013-02-07.pdf). Accessed 24 Jan 2023.
65. G. Stechauner and E. Kozeschnik: *Calphad*, 2014, vol. 47, pp. 92–9.
66. J. Kreyca and E. Kozeschnik: *Int. J. Plast.*, 2018, vol. 103, pp. 67–80.
67. H. Mecking and U.F. Kocks: *Acta Metall.*, 1981, vol. 29, pp. 1865–875.
68. U.F. Kocks and H. Mecking: *Prog. Mater. Sci.*, 2003, vol. 48, pp. 171–273.
69. E. Sobotka, J. Kreyca, M.C. Poletti, and E. Povoden-Karadeniz: *Materials*, 2022, vol. 15, p. 6824.
70. E. Kozeschnik: *Metall. Mater. Trans. A*, 2000, vol. 31A, pp. 1682–684.
71. E. Kozeschnik, W. Rindler, and B. Buchmayr: *Int. J. Mater. Res.*, 2007, vol. 98, pp. 826–31.
72. W. Rindler, E. Kozeschnik, and B. Buchmayr: *Steel Res.*, 2000, vol. 71, pp. 460–65.
73. M. Rath and E. Kozeschnik: *MSF*, 2013, vol. 753, pp. 357–60.
74. E. Sobotka, J. Kreyca, R. Kahlenberg, A. Jacob, E. Kozeschnik, and E. Povoden-Karadeniz: *Metals*, 2023, vol. 13, p. 884.
75. M. Lückl, S. Zamberger, and E. Kozeschnik: *Steel Res. Int.*, 2016, vol. 87, pp. 271–75.
76. Y.M. Kim, H. Lee, and N.J. Kim: *Mater. Sci. Eng. A*, 2008, vol. 478, pp. 361–70.
77. H. Zhao and E.J. Palmiere: *Mater. Charact.*, 2019, vol. 158, p. 109990.

**Publisher's Note** Springer Nature remains neutral with regard to jurisdictional claims in published maps and institutional affiliations.